ECAP-2019-001

Master's Thesis in Physics

Phase-Contrast Imaging in the Optical Wavelength Regime

Presented by
Bernhard Akstaller
28 February 2019

Erlangen Centre for Astroparticle Physics
Department of Physics
Friedrich-Alexander Universität Erlangen-Nürnberg

Supervisor: Prof. Dr. Stefan Funk

Contents

1 Introduction

After it has been upgraded to start its second run in 2015, the Large Hadron Collider is capable of accelerating particles to an energy of 16 TeV [CER19]. This remarkable energy is surpassed by orders of magnitudes by galactic particle accelerators [Hes16]. Phase-contrast X-ray imaging is a promising candidate for the study of processes that are envolved in the acceleration of such high-energy particles. X-ray imaging started off in November 1895, when Wilhelm Conrad Röntgen discovered that cathode ray tubes produce a radiation, which penetrates solid objects and colors photograpic plates [Rö96]. Not even two months later, he had recorded images of multiple objects and, most famously, of his wife's hand [Deu99]. The new imaging technique had far reaching consequences for scientific research, medical diagnostics and non-destructive testing.

Knowledge about the means to manipulate the path of light dates a long time back. A reference to burning lenses can be found in an ancient Greek comedy from 424 B.C. [Hec14]. With such means, Hooke presented a technique to visualize the phase-contrast caused by the temperature gradient in hot air above a candle in the year of 1672 [Set01]. The Talbot effect, which is the basis of an X-ray phase-contrast technique, was discovered in an optical experiment in 1836. Phase-contrast imaging is based on diffraction and interference phenomena, which are properties of electromagnetic radiation. Whether the photon energies lie in the optical or in the X-ray regime, plays no role in that. In the X-ray regime however, research on Talbot interferometry is often limited to polychromatic laboratory tubes, since access to coherent and monochromatic synchrotron radiation is rare. But in the optical regime, lasers have properties equivalent to synchrotrons. So it is desirable to apply the established X-ray phase-contrast methods to an optical experiment.

The experiments that are prepared, described, conducted and evaluated in this thesis are designed to test and compare three different phase-contrast imaging techniques for conditions that model possible experiments in the field of laboratory astrophysics. To that end, butane gas jets are imaged with an Talbot interferoemter, with in-line phase-contrast and with a Schlieren set-up.

2 Theory

In optical phase-contrast imaging visible light is employed to probe a transparent sample. Retrieving the optical properties of these samples is the main aspect of this thesis. Although the presented experiments utilize gas jets, the long-term perspective is to work towards plasma experiments with relevance for laboratory astrophysics. This chapter discusses the interaction between the sample and the electromagnetic waves of the probe beam. A description of wave propagation in matter is followed by an explanation for the emergence of phase-contrast in plasma. After a short excursion to experiments in the field of laboratory astrophysics, a selection of phase-contrast imaging techniques is presented.

2.1 Electromagnetic Waves in Matter

The behavior of electric fields E and magnetic H fields in matter or vacuum can be described by the macroscopic Maxwell's equations. The discussion in this chapter follows the standard text books [Dem17, Mes17, Dem11, Hec14]. The Maxwell's equations in isotropic dielectric matter can be given as

$$\begin{aligned} \vec{\nabla} \cdot \vec{D} &= \rho_e & \vec{\nabla} \times \vec{E} &= \frac{\partial \vec{B}}{\partial t} \\ \vec{\nabla} \cdot \vec{B} &= 0 & \vec{\nabla} \times \vec{H} &= \vec{\nabla} \cdot \vec{j} + \frac{\partial \vec{D}}{\partial t}\,, \end{aligned}$$

where $\vec{D}$ is the dielectric displacement, $\vec{B}$ is the magnetic field in the material, ρ_e is the electric charge density and $\vec{j}$ is the current density vector. The displacement is given by $\vec{D} = \epsilon_0 \epsilon_\mathrm{r} \vec{E}$ and $\vec{B} = \mu_0 \mu_\mathrm{r} \vec{H}$, where ϵ_0 and ϵ_r are the free space and the relative electric permittivity and μ_0 and μ_r are the vacuum and the relative magnetic permeability. The unitless quantities ϵ_r and μ_r model the microscopic properties of the medium. This will be considered in more detail in Section 2.2.1.

A direct consequence of Maxwell's equations is the propagation of electromagnetic waves. Using the vector identity $\vec{\nabla} \times (\vec{\nabla} \times \vec{E}) = \vec{\nabla}(\vec{\nabla} \cdot \vec{E}) - \vec{\nabla}^2 \vec{E}$, the wave equation for $\vec{E}$ can be derived as

$$\left(\vec{\nabla}^2 - \epsilon\mu \frac{\partial^2}{\partial t^2} \right) \vec{E} = 0 \,, \tag{2.1}$$

where $\epsilon = \epsilon_0 \epsilon_\mathrm{r}$ and $\mu = \mu_0 \mu_\mathrm{r}$. The wave equation of $\vec{B}$ can be derived analogously. The general solution of Equation 2.1 can be formulated as a superposition of plane waves. A plane wave is given by

$$\vec{E}(\vec{r}, t) = \vec{E}_0 \cdot e^{i(\vec{k}\vec{r} - \omega t)}, \tag{2.2}$$

where $\vec{E}_0$ is the vector-valued electric field amplitude, $\vec{k}$ is the wave vector and $\omega = 2\pi\nu$ is the angular frequency, where ν is the oscillation frequency of the electromagnetic wave. The wave vector gives the direction of propagation which, for plane waves, is perpendicular to the directions of $\vec{E}$ and $\vec{B}$. It can be written as

$$\vec{k} = \omega \, (\vec{E} \times \vec{B}).$$

In the optical regime, the wavelength is typically used to characterize light. For X-rays, the photon energy in electron volts is a more convenient quantity. However, since this thesis is mainly about an optical experiment, the wavelength picture will be used.

In Equation 2.1, the time differential is multiplied by the factor $\epsilon\mu$. This factor in the wave equation gives the velocity at which the electromagnetic waves spread in a medium. It can be split up in the vacuum speed of light $c_0 = (\epsilon_0 \mu_0)^{-0.5}$ and the complex refractive index $\tilde{n} = \sqrt{\epsilon_\mathrm{r} \mu_\mathrm{r}}$ which models the optical properties of the medium. $\tilde{n}$ equals 1 in vacuum and can be larger or smaller than 1 in a medium. If $\tilde{n}$ depends on the wavelength, the medium is called dispersive. In Section 2.2.1, it is shown that $\tilde{n}$ is a complex quantity

$$\tilde{n} = n + i\,\kappa \,, \tag{2.3}$$

with the real part n and the imaginary κ part of the refractive index.

The phase velocity c_{ph} is the velocity at which the phase fronts of the light propagate. It can be given in different forms

$$c_{\mathrm{ph}} = \frac{\omega}{k} = \lambda\,\nu\,,$$

where the scalar wave number $k = 2\pi/\lambda = |\vec{k}|$ and the wavelength λ are used. Inserting the refractive index gives the relations for the vacuum wavelength λ_0, the vacuum wave number k_0 and the phase velocity in the refractive medium

$$c_{\mathrm{ph}} = \frac{c_0}{\tilde{n}}\,, \qquad k_0 = \frac{k}{\tilde{n}}\,, \qquad \lambda_0 = \tilde{n}\,\lambda\,. \tag{2.4}$$

On a side note, it should be pointed out that the phase velocity must not be confused with the so-called group velocity. Since n can be smaller than 1, c_{ph} may exceed the speed of light. However, the speed of the flow of energy and information is given by the group velocity which is always below c in accordance with the theory of relativity.

In order to calculate the phase delay caused by a change in the refractive index, the wave vector is chosen as $\vec{k} = (0, 0, k)$ to define z as propagation direction of $\vec{E}(r_z, t)$, with the z-component r_z of $\vec{r}$. With this, the complex refractive index from Equation 2.3 and k_0 from Equation 2.4, Equation 2.2 can be written as

$$\vec{E}(r_z, t) = \vec{E}_0 \cdot e^{i\,(k_0 n r_z - \omega t)}\, e^{-\kappa k_0 r_z}\,. \tag{2.5}$$

The exponential $e^{-\kappa k_0 r_z}$ that describes the envelope of the wave is a real-valued exponential. The intensity of a light wave is calculated as the square of the absolute value of its electric and magnetic field components. The imaginary exponentials in the equation all cancel out in an absolute square. So, the envelope of the wave is the only part in Equation 2.5 that contributes to the electromagnetic intensity. The imaginary part κ of the refractive index is therefore also referred to as extinction coefficient. It is a measure for the light attenuation in a medium.

The exponential $e^{i\,(k_0 n r_z - \omega t)}$ in Equation 2.5 is a plane wave where the wave number k_0 is scaled by n. This scaling is illustrated in Figure 2.1. Two equivalent plane waves propagate a certain path length Δz through two regions of different refractive indices. $\Delta\Phi$ is the accumulated phase difference after this length. It can be calculated by

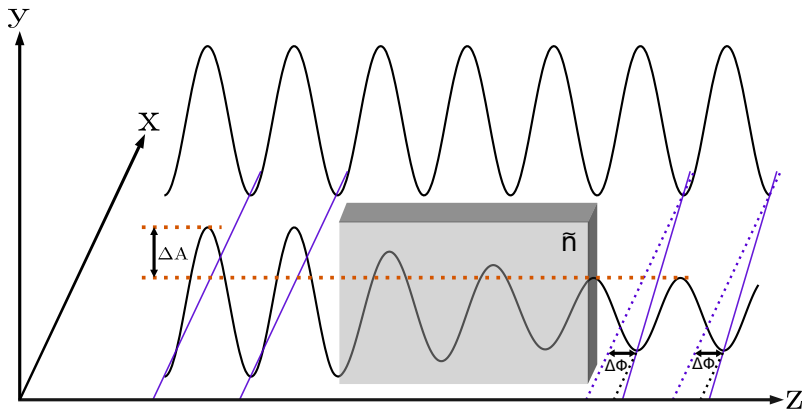

Figure 2.1: Schematic of a plane wave propagating in z-direction through a medium with complex refractive index $\tilde{n}$ as compared to another wave propagating in vacuum. The blue lines connect points of equal phase in both waves. While traversing the medium with $\tilde{n}$, the wave accumulates a phase-shift $\Delta\Phi$. Absorption causes a reduction of the amplitude which is marked by ΔA. The figure is adapted from [Sch16].

$$\Delta\Phi = (n_2 - n_1) \cdot k_0 \Delta z, \tag{2.6}$$

where n_1 is the real part of the refractive index of the regarded medium and n_2 of the surrounding medium. This shows that phase-contrast emerges from variations of the refractive index in the medium. Measuring this phase-contrast to retrieve these variations within a test object is the subject of Chapter 2.3.

2.2 Plasma

The derivation of the propagation of light in a medium in Section 2.1 assumes certain material properties. How these properties emerge in a material is discussed in this section on the example of plasma, which is a neutral gas consisting of charged particles [Fox12]. Further, the phase-shift in plasma is discussed and measurements of laser produced plasma shock waves are briefly addressed.

2.2.1 The Refractive Index of Plasma

The refractive index, as introduced in Section 2.1, can be used to describe the influence of the macroscopic material properties on light propagation. Here, the goal

is to link these macroscopic properties to a microscopic description of the medium. Based on [Fox12], the influence of the material on wave propagation is discussed, starting from the Lorentz model.

In dielectric media, the atoms are modeled as dipoles with an angular resonance frequency ω_0. Light acts as an oscillating external force on such dipoles, driving a forced oscillation. If the angular frequency of the incident light ω is sufficiently close to ω_0, the dipoles behave like Lorentz oscillators. While oscillating, the electrons of the atom are displaced from their equilibrium position. This displacement causes a polarization of the medium, which depends on the number of atoms per unit volume N, the electron mass m_0 and charge e as well as the damping constant from the Lorentz model γ. In near-resonant approximation, the resonant polarization is then given as

$$P_{\text{resonant}}(\omega) = \frac{N\,e^2}{m_0} \cdot \frac{E}{\omega_0^2 - \omega^2 - i\gamma\omega}, \tag{2.7}$$

where E is the absolute value of the driving electric field. Close to the resonance frequency, P_{resonant} gives a large contribution to the dielectric displacement D. Another contribution is the background polarization $P_{\text{background}}$. It stems from other sources of polarization or further resonances at much higher frequencies. With this, the dielectric displacement can be written as

$$D = \epsilon_0 E + P_{\text{resonant}} + P_{\text{background}}\,. \tag{2.8}$$

From the definition in section 2.1, the scalar formulation of the displacement can be derived to $D = \epsilon_\text{r}\epsilon_0 E$. With this as well as the two Equations 2.7 and 2.8, the relative permittivity ϵ_r is already implicitly defined. In a dielectric material it can be written as

$$\epsilon_\text{r}(\omega) = 1 + \frac{P_{\text{background}}}{\epsilon_0 E} + \frac{N\,e^2}{\epsilon_0\,m_0}\,\frac{1}{\omega_0^2 - \omega^2 - i\gamma\omega}\,. \tag{2.9}$$

The background polarization and the resonance frequency were derived from the resonant behavior of the electrons. However, in contrast to electrons in dielectric materials, free electrons have no defined equilibrium position and thus experience no restoring force. Plasmas are made up of free charge carriers. So, the background

polarization and the resonance frequency give no contribution to the relative permittivity of a plasma, which thus simplifies to

$$\epsilon_{\mathrm{r,pl}}(\omega) = 1 - \frac{N_e\, e^2}{\epsilon_0\, m_0}\, \frac{1}{\omega^2 + i\gamma\omega}\,, \tag{2.10}$$

where N_e is the electron density. For weak coupling in the plasma the damping can be neglected. Accordingly, the damping constant γ is set to zero, so that Equation 2.10 becomes

$$\epsilon_{\mathrm{r,pl}}(\omega) = 1 - \frac{\omega_\mathrm{p}^2}{\omega^2}\,, \tag{2.11}$$

with the plasma frequency ω_p, which describes the normal mode frequency of the plasma and is given by

$$\omega_\mathrm{p} = \sqrt{\frac{N_e\, e^2}{\epsilon_0\, m_0}}\,. \tag{2.12}$$

The influence of the magnetic permeability μ_r is usually small. A common approximation is $\mu_\mathrm{r} = 1$, so that the refractive index is $\tilde{n} = \sqrt{\epsilon_r}$. By inserting Equation 2.11 in this, the refractive index of a plasma is obtained as

$$\tilde{n}_\mathrm{pl} = \sqrt{1 - \frac{\omega_\mathrm{p}^2}{\omega^2}}\,. \tag{2.13}$$

The plasma frequency and $\tilde{n}_\mathrm{pl}$ manifest in the optical properties of a plasma. An important property is the reflectivity which is calculated from the real part of $\tilde{n}$ by $R = |(n-1)/(n+1)|^2$. A plot of R for a plasma can be seen in Figure 2.2. Since $\tilde{n}$ is purely imaginary for $\omega < \omega_\mathrm{p}$, the plasma has a reflectivity of $R = 1$ in this region. Above the plasma frequency the plasma becomes transparent. With Equation 2.13, a link between fundamental material properties and optical characteristics of a plasma is found.

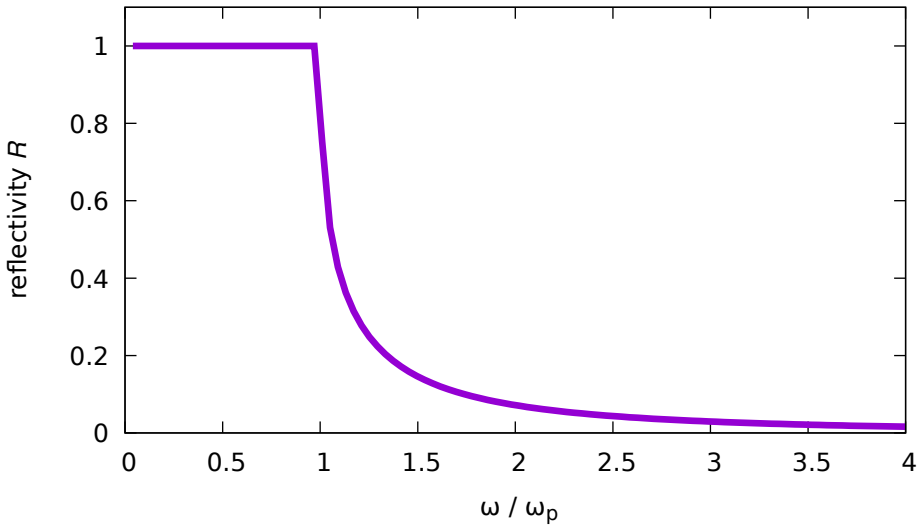

Figure 2.2: The reflectivity of a plasma with weak coupling is plotted over the optical frequency ω of the impinging light. For $\omega < \omega_\mathrm{p}$, R is approximately 1. Above ω_p however, R drops and the plasma becomes transparent. The plot is adapted from [Fox12].

2.2.2 Phase-Shift of Waves in Plasma

The refractive index of plasma links the phase-shift and the electron density of the plasma. The plasma is transparent for light of much higher frequencies than ω_p. In this regime, $\tilde{n} = n$. A first order Taylor expansion around $\omega \to \infty$ of the refractive index from Equation 2.13 can be given as

$$n \approx 1 - \frac{\omega_p^2}{2\omega^2}\,.$$

From this and Equation 2.6, together with the definition of the plasma frequency in Equation 2.12, the phase-shift can be calculated to

$$\begin{aligned}\Delta\Phi_e &= \Delta n k_0 L \\ &= (1 - \frac{\omega_p^2}{2\omega^2} - 1) k_0 L \\ &= -\frac{2\pi}{\lambda_0} L \frac{N_e e^2}{\epsilon_0 m_0} \frac{\lambda_0^2}{2(2\pi)^2 c_0^2} \\ &= -L N_e r_e \lambda_0 \,,\end{aligned}$$

with the classical electron radius $r_e = e^2/(4\pi\epsilon_0 \cdot m_0 c_0^2)$. $\Delta\Phi_e$ is the contribution to the phase-shift due to plasma electrons with the line-integrated electron number density LN_e [WF97]. In the presence of another gas with a density ρ_0, the electrons bound in the gas molecules can contribute to the refractive index as well [DZ18]. This contribution to the phase-shift is given by [WF97]

$$\Delta\Phi_n = \frac{2\pi}{\lambda} \frac{n-1}{\rho_0} \rho_\mathrm{L} L \,,$$

with the integrated neutral number density $\rho_\mathrm{L} L$. Since $\Delta\Phi_e$ and $\Delta\Phi_n$ scale differently with the wavelength, they can be determined separately by use of so-called two color interferometry [WF97, Job95]. This has not been conducted in the experiments for this thesis, since the tested objects consists completely of neutral gas. However, two-color interferometry can be applied in experimental set-ups for laboratory astrophysics and will be part of the discussion in the next subsection.

2.2.3 Experiments in Laboratory Astrophysics

The equations describing astronomical processes can be mapped to the microscopic scale of laser-based plasma experiments in the laboratory. The results of such experiments can then be mapped back to get an insight to the nature of certain mechanisms in the cosmos [Rem05]. There are experiments based on laser generated plasmas that model accretion discs [HB02], the formation of supersonic plasma jets [LCB+02] or particle acceleration in shock waves occurring in supernova remnants [RAP+99]. However, laboratory astrophysics is only one part of the much larger field of plasma research. Other important parts are fusion ignition [CSJ+18, VSF13] or plasma accelerators [DZ18, MGA+96, CSJ+18]. With a brief overview over some plasma experiments, this section is aimed to give an idea of typical parameters in realistic set-ups.

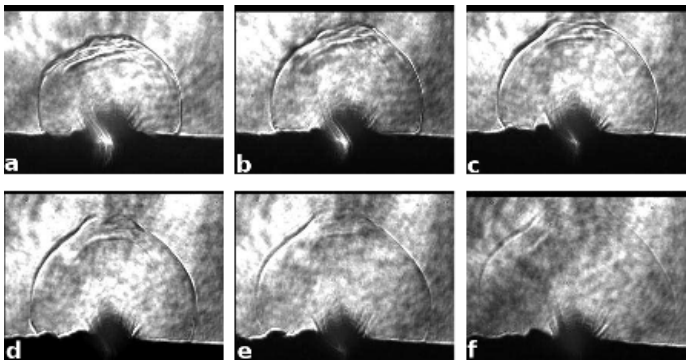

Figure 2.3: Shadowgraphy of plasma plume produced by a high-power laser on an aluminum target. The target was placed in a nitrogen chamber, the gas pressure gradually decreases from image a to image f. Adapted from [Gre07].

Different methods can be applied to probe the phase-contrast emerging in plasma shock waves. This can be used to research processes occurring in high-density plasma experiments. The imaging technique shadowgraphy, which will be discussed in more detail in Section 2.3.4, is a possible candidate for plasma diagnostics [Gre07]. In the experiment described in [Gre07], a solid aluminum target, that is placed in a nitrogen gas container, is irradiated by a high-power laser. The sudden heat from the laser produces a supersonic plasma plume, which can be seen in Figure 2.3. To probe the plume, the picosecond pulsed infrared drive laser is shifted in frequency. In the plasma plume a shock front with sharp density features forms. As mentioned, the features are visualized using shadowgraphy. This allows some insight to the propagation of the shock in an ambient gas.

The phase-contrast in plasma can be imaged interferometrically as well. This poses an alternative to the grating-based or propagation-based approaches, that are used in the measurements for this thesis. An experiment that uses interferometry is presented in [WAC+04]. There, two plastic foils, that are placed in a strong magnetic field, are used as targets. They face each other at a distance of 1 mm. A pump laser simultaneously hits the targets, forming two counter-streaming plasma plumes with an electron density of up to $10^{18}\,\mathrm{cm}^{-3}$. In the central area between the foils, the conditions in a supernova remnant are simulated. An outcoupled, frequency shifted probe laser pulse is used for interferometric plasma diagnostic. The experiment researches the influence of a magnetic field on a collisionless plasma. The shock waves in supernova remnants are collisionless because of the low particle densities in the interstellar medium [DWYT15].

A similar experiment is described in [PRH+16]. Again, two plastic foils are used as target to produce collisionless counter-streaming plasma. Instead of interferometry however, Thomson scattering diagnostics is used. The probe beam is focused on the

central region between the foils. The Thomson-scattered light from this region is collected to measure the electron temperature and density. Further, the ion temperature and bulk plasma flow velocity can be obtained as well. Electron densities of up to $10^{19}\,\mathrm{cm}^{-3}$ are reported.

The parameters of the experiments lie within a wide range with some experiments reaching a temporal resolution of tens of femtoseconds and a spatial resolution of up to a few microns [Fiu15]. Lasers in the optical and near infrared wavelength range are used. As a direct measure of the electron density, phase-contrast plays an important role in the experiments. Different imaging techniques will be the main aspect of Chapter 2.3.

2.3 Phase-Contrast Imaging

Phase-contrast imaging allows the retrieval of a phase-shift caused by transparent objects. This section discusses different phase-contrast imaging techniques. While the focus lies on the optical regime, X-ray phase-contrast imaging is addressed as well.

2.3.1 Grating-Based Phase-Contrast Imaging

The Talbot effect is a near field diffraction phenomenon occurring at periodic structures that are illuminated with sufficient spatial coherence [SWX+11]. So, optical gratings are used for Talbot interferometry in the experiments. Commercially available gratings are either reflective or transmitting, structured in one or in two dimensions. They either modulate the light amplitude or the phase. After a short outline on such gratings, this section gives an introduction to the Talbot effect and the method of Fourier imaging.

Amplitude Grating

The so-called absorption or amplitude grating alters the amplitude of the traversing light. This modulation can be achieved by a layer of periodic, absorbing lines on a transparent carrier, or it by an opaque plate with regular slits in it. The relation between the structure period and the width of the slits is called duty cycle. Per definition, the duty cycle is 1 for a grating that absorbs all light, 1/2 if the bars are as wide as the slits in between and 0 if the grating absorbs no light. After traversing the grating, the light shows a characteristic interference pattern. In the far field,

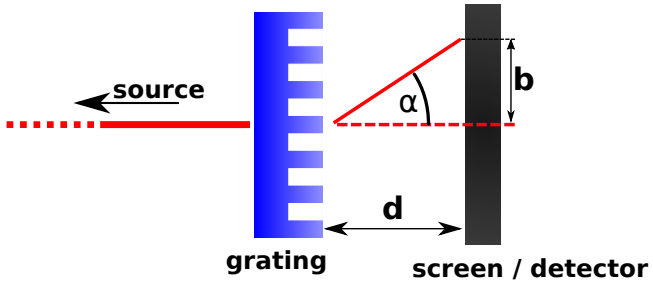

Figure 2.4: Sketch of a grating's far field diffraction pattern as seen by a detector. The 650 nm laser beam (red) originates from a distant source. The beam is split up in the grating into multiple diffraction orders. The distance from screen to detector is d and the spacing from the zeroth $m_d = 0$ to the first $m_d = +1$ diffraction order on the screen is b, with the corresponding diffraction angle α. The sketch is not in scale.

the pattern is described by the grating equation. For the simplified case of light at normal incidence, according to [PPBS96], the diffraction formula can be given as

$$\sin(\alpha) = \frac{m_d \, \lambda}{p} \,, \tag{2.14}$$

where α is the angle of diffraction, p the grating period and $m_d \in \mathbb{Z}$ is the order of diffraction. A sketch for this is shown in Figure 2.4. This also describes a method to measure the grating period, if λ is known. The implementation of this measurement is described in Section 4.3.2.

Phase Grating

Transmission phase gratings consist of a transparent material with a periodically structured surface. The surface imprints a modulation on the phase-fronts of light. An ideal phase grating absorbs no light, which can be advantageous over amplitude gratings. Every photon that is lost within the grating cannot contribute to the signal, which potentially has a negative influence on the signal-to-noise ratio [Bec09]. Furthermore, in X-ray applications, it can be difficult to manufacture the small grating structures sufficiently thick to fully absorb hard X-rays, as is required for amplitude gratings. This favors phase gratings for X-ray Talbot imaging with high energies [CGM+97].

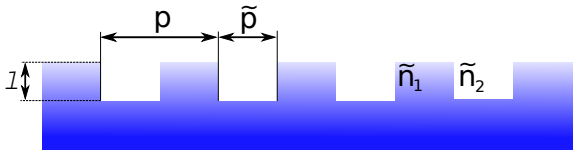

Figure 2.5: Sketch of a binary phase grating with a periodicity of p and a duty cycle of $\tilde{p}/p$. The depth of the bars is l, the refractive index is $\tilde{n}_1$ in the grating material and $\tilde{n}_1$ in the surounding medium. The sketch is adapted from [PPBS96].

While there are multiple common shapes of phase gratings [Tho18], this work only considers the so-called binary phase grating design as sketched in Figure 2.5. It consists of a material with refractive index n_1, which is surrounded by a medium with n_2. So, the phase velocities in the two media differ. Due to the grating bars on the surface, the optical path length varies between the light that passes the bars and light that passes through the gaps in between. Consequently, there is a transient area where a part of the wave moves faster, which distorts the phase fronts. The height of this imprinted shape is called phase depth $\Delta\Phi$ and can be given as [EGP07]

$$\Delta\Phi = 2\pi l \, \frac{n_1 - n_2}{\lambda} \,, \tag{2.15}$$

where l is the depth of the grating structure, which is indicated in Figure 2.5.

Gratings with $\Delta\Phi = \pi$ show a special property in the far field. Light passing through the gaps of the grating is shifted by π compared to light that passes through the bars. This leads to a suppression of the zeroth diffraction order in the far field, because there the two contributions, that are opposite in phase, overlay directly [Buc07]. The properties of the π-shifting phase grating in the near field are mentioned at the end of the next section.

The Talbot Effect

If a plate with an array of equidistant slits is illuminated by a small point source of white light, an image of the slits forms at certain distances behind the plate. This was first observed in the year 1836 and is nowadays known as Talbot effect, named after its discoverer [Tal36]. Talbot further found, that the so-called Talbot distance, at which the first self image forms, is different for every color. 45 years later Lord Rayleigh found a mathematical description for this effect, after he repeated Talbot's experiments. He described the Talbot distance as [Lor81]

$$Z_T = \frac{\lambda}{1 + \sqrt{1 - \lambda^2/p^2}} ,$$

with the optical wavelength λ and the grating period p. Since p is small compared to λ, a sufficient approximation for the Talbot distance is [Lor81]

$$Z_T = 2\,\frac{p^2}{\lambda} .$$

The Talbot distance is also a measure for the periodicity of this effect. Further self images can be found at the positions [Edg69]

$$Z_T^m = m \cdot Z_T \ , \qquad m \in \mathbb{N} .$$

For unambiguousness, Z_T is also referred to as full Talbot distance. Within each full distance, further self images of the grating can be found. For amplitude gratings, they are translated by a half period perpendicular to the orientation of the grating bars in the transverse plane. The fractional Talbot pattern of an amplitude grating lies in the center of each full Talbot distance, which can be expressed by [Edg69]

$$Z_H^m = (2m - 1)\,\frac{d^2}{\lambda} .$$

Phase gratings produce multiple intermediate self images at the distances $Z_F^{\tilde{m}}$, given by [YWL15]

$$Z_F^{\tilde{m}} = \frac{2\tilde{m} - 1}{4\,\eta^2} \cdot Z_T \ , \qquad \tilde{m} \in \mathbb{N} ,$$

with $\eta \in \{1, 2\}$ accounting for the scaling with different gratings. For π-shifting phase gratings this factor is set to $\eta = 2$. So, there are 8 fractional Talbot distances within every Talbot distance. For $\pi/2$ phase gratings it is set to $\eta = 1$, which gives only 2 fractionals in Z_T [YWL15]. Also for π-shifting phase gratings, the frequency of the transverse modulation in the Talbot image is doubled [Sul97]. The transition from regular Talbot images to the frequency doubled images is illustrated by the simulations in Section 3.4.

Fourier Imaging

The Talbot effect described above can be utilized for phase-contrast imaging. As discussed in Section 2.2.2, local variations of the refractive index in a medium distort the phase fronts of a probe beam. This has an influence on the form of the wave fronts incident on the Talbot grating, which then deforms the Talbot pattern [SGL+18]. Thus, the phase-shift is transformed into variations of the intensity distribution, which can be detected by an imaging sensor. Those changes are analyzed to obtain the attenuation, the small-angle scattering and the phase-shift caused by the transparent object. Three image modalities are thereby retrieved, namely attenuation, differential phase-contrast and the object's dark-field property [SGL+18].

To calculate the image modalities, two measurements with the Talbot interferometer are necessary. The so-called reference image, labeled by an index *ref*, is taken without an object in the interferometer to capture the image modalities of the interferometer without an object. The second image is taken with an object in the interferometer and labeled by the index *obj*. It has contributions of the empty interferometer and the object. The task of Fourier imaging is to separate these contributions and to retrieve the image modalities. Apart from the reference image, Fourier imaging requires only one image for every object measurement which is why it is considered a single-shot method.

The Talbot pattern ideally forms a perfect self-image of the grating bars, which are orientated in the y direction. The intensity distribution $I(x, y)$ of the image can be given as [TIK82]

$$I(x, y) = I_0(x, y) + I_1(x, y) \cos\left[2\pi f_0 x + \Delta\phi(x, y)\right] , \tag{2.16}$$

with the overall intensity $I_0(x, y)$, the oscillation intensity $I_1(x, y)$ and the grating's spatial frequency f_0. This describes the intensity distribution produced by an amplitude grating with a sinusoidal modulation. For rectangular, binary gratings, Equation 2.16 is only an approximation. It represents the first two terms of the intensity pattern's Fourier expansion [BZL+12]. The transmitivity of the object is coded in the attenuation image $T(x, y)$. It is obtained from the intensity $I_{0,\mathrm{obj}}$ of the object image and the intensity $I_{0,\mathrm{ref}}$ of the reference image as follows

$$T(x, y) = -\ln\left[\frac{|I_{0,\mathrm{obj}}(x, y)|}{|I_{0,\mathrm{ref}}(x, y)|}\right] .$$

The relation between the intensity of the bright and dark stripes in the image is called visibility $V(x, y)$ and defined by [EKB+08] as

$$V(x, y) = \frac{I_{\max} - I_{\min}}{I_{\max} + I_{\min}}, \tag{2.17}$$

where $I_{\max}$ is the maximum and $I_{\min} > 0$ the minimum intensity of the interference pattern. For sinusoidal intensity fringes, this is equivalent to the definition used by [BZL+12]. There the visibility is defined as the relation between constant and oscillating intensity

$$\tilde{V}(x, y) = \frac{|I_1(x, y)|}{|I_0(x, y)|}.$$

If not stated otherwise, the definition in Equation 2.17 is used in this thesis. The visibility is 1 for a perfect interferometer and 0 if no variation is detectable. The imperfections of a real interferometer reduce the visibility, making it an indicator of the interferometer's quality [Bar10]. In addition, the visibility characterizes the small angle scattering occurring in the object [BKSW10]. This is the so-called dark-field signal D which is given by the relation of the visibility with object V_{obj} and without object V_{ref} in the interferometer as follows [BZL+12]

$$D \;=\; -\ln\left[\frac{V_{\text{obj}}}{V_{\text{ref}}}\right].$$

While the dark-field signal is caused by changes in the refractive index, that are smaller than the spatial resolution of the interferometer, changes on a larger scale are detected as phase-shift [SLG+18].

Since the grating's spatial frequency f_0 is much higher than the frequencies in the modulations of $I_0(x, y)$, $I_1(x, y)$ or $\Delta\phi(x, y)$, they are separated in the Fourier space [TIK82]. As an example, one line of a Fourier transformed image is shown in Figure 2.6. It mainly consists of three peaks, with the central peak containing the low-frequency information of the image and the two outer peaks containing the grating information. To find the lateral shift of the grating bars, the central peak is removed and one of the outer peaks is shifted by f_0 towards the origin. This spectrum is then processed with the inverse Fourier transform to get the image back into real space. There, the differential phase $\phi(x, y)$ and the amplitude variation I_1 of the

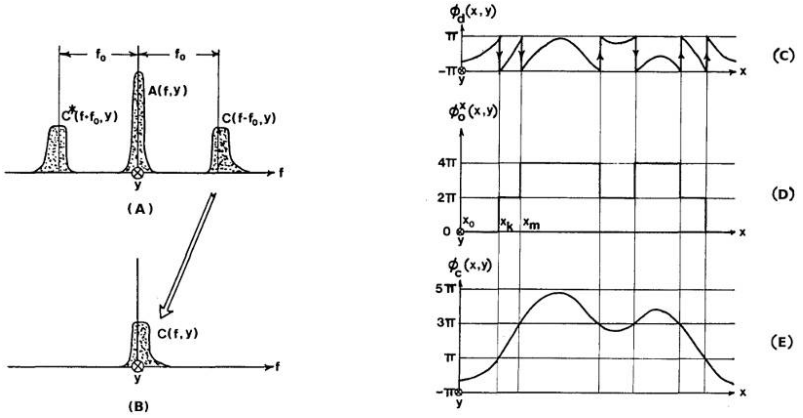

Figure 2.6: Graphic on the left: Fourier spectrum of the Talbot image before and after applying frequency cut and shift. In plot (A) the separation of the peaks by f_0 is clearly visible. In plot (B) the peak at $+f_0$ is shifted to the origin. Graphic on the right: Example for the unwrapping procedure. (C) is the wrapped input, (D) shows the offset, that increases by 2π if the input jumps down and decreases by 2π for positive jumps. Finally, input and offset add up to the unwrapped signal which is plotted in (E). The plots are adapted from [TIK82].

pattern [TIK82] are separated as a consequence of this procedure. As described earlier, the phase-shift $\Delta\phi$ induced by the object is acquired from the two images by

$$\Delta\phi \;=\; \phi_{\mathrm{obj}} \;-\; \phi_{\mathrm{ref}}\,,$$

where ϕ_{ref} is the phase of the empty interferometer and ϕ_{obj} the phase obtained from the object measurement. This phase information is only defined modulo the factor 2π [TIK82]. An example for this is shown in Figure 2.6. The otherwise smooth phase-shift exhibits discontinuous jumps of $\pm 2\pi$. These discontinuities can be fixed by adding or subtracting an offset depending on the sign of the jump. The procedure is described in more detail in [TIK82]. It is furthermore sketched in Figure 2.6 and will be referred to as unwrapping. After correcting the differential phase-shift $\Delta\phi$ for wrapping, it can be integrated in x-direction to approximately yield the phase-shift $\Delta\Phi$ induced by the whole object [Rit15]

$$\Delta\Phi \;\approx\; \frac{kd}{2\pi}\,\frac{1}{\delta x}\int \Delta\phi\,\mathrm{d}x$$

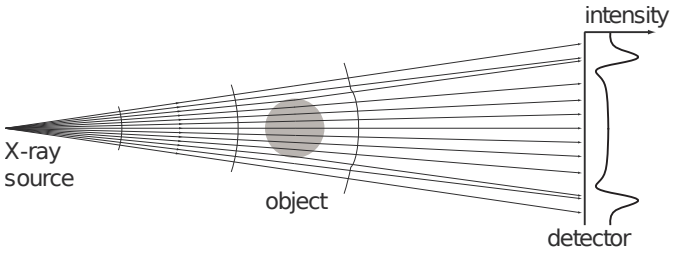

Figure 2.7: Principle of X-ray in-line holography. A coherent source with spherical wavefront irradiates a phase-shifting object. The distorted wavefront propagates on to the detector where the intensity distribution is imaged with distinct edge-enhancement. The figure is taken from [BLT+11].

where d is the distance from the Talbot grating to the detector and δx is the size of the detector pixels.

Many imaging applications require a high spatial resolution. This is the case for example in clinical X-ray imaging applications, where the resolution of the area X-ray detectors is critical [WDD+05]. There are grating-based approaches to enhance the spatial resolution of the reconstructed phase-contrast images, namely phase-stepping [WDD+05] and moire-imaging [SGL+18]. Both techniques require an additional grating. In phase stepping, multiple images are taken of the same object with the additional grating set at different positions. So the method is best suited for static or slowly moving objects. In moire-imaging, the additional grating is tilted to form a moire-pattern which has a larger period than the gratings itself. Thus, the grating can be chosen finer than the detector resolution. Since only one image is required for this, moire-imaging would be suited for imaging fast processes like shock waves in plasma. However, neither of these methods have been applied to the optical set-up in this work so far.

In addition to the gratin-based approach of phase-contrast imaging, this work also addresses methods that are based on propagation effects to image phase-contrast. The working principles are outlined in the following sections.

2.3.2 Propagation-Based In-Line Holography

As discussed in Section 2.1, the real part of the refractive index does not describe the absorption of light, but the influence on the phase. Transparent objects disturb the wave fronts and produce characteristic intensity distributions after certain propagation distances [Pag06]. Using so-called in-line holography algorithms, this can be calculated back to retrieve the phase-contrast induced by the object [BLT+11].

The basic principle of in-line holography is sketched in Figure 2.7. A small source spot illuminates a phase-shifting object and the detector. Even a source with low temporal coherence can be used, as long as spatial coherence is sufficient [WGG+96]. For example, an X-ray tube with a tiny focus spot serves for this task. In order to conduct in-line holography, an object is illuminated by the source and the disturbed light field propagates for a long distance, forming a intensity distribution due to Fresnel diffraction [BLT+11]. The object's optical properties can be reconstructed from the detected intensity images [CPP+10]. Among other methods, iterative back-propagation algorithms are utilised for such reconstructions. They require prior knowledge about the object properties, which can be incorporated by choosing the according constrains. This can be available information of the problem like the size of the object, its chemical composition or the distances between source, object and detector. What constraints are required depends on the algorithm chosen according to the specific task [HS17, SHM+15, GKK+11, CPP+10]. But nevertheless, the basic principle is the same for all of them. The object's optical properties are modeled by the so-called transmission function, which has certain free parameters. The wave's propagation in free space between object and detector is modeled by the so-called propagation operator. The algorithms start off by guessing the parameters of the transmission function. Next, the propagation of the disturbed waves to the detector is calculated. Thereby, the resulting image can be compared to the actually measured intensity image. This information is used to alter the object properties accordingly. From that on, the procedure starts again with the updated transmission function with the aim to further reduce the deviations between calculated and measured image. This iterative procedure is conducted until the deviations become sufficiently small.

2.3.3 Schlieren Imaging

Schlieren imagig is an optical phase-contrast technique that has been demonstrated by Hooke in the year 1672 [Set01]. The principal technique and a possible design for an experimental set-up are outlined in this section according to the description in [Set01].

The term Schliere refers to a gradient disturbance of an inhomogeneous optically transparent medium. Schlieren objects have a different refractive index compared to the surrounding medium. For instance, such an object can be an inhomogeneity in glass, a sound wave in water, the mixing of two different liquids, a gas jet in air, or pressure and temperature gradients in a medium. In the Schlieren set-up in Figure 2.8, such an object is placed in a parallel light beam. A part of the light is slightly deflected away from the original path. Behind the object, the beam is focused onto

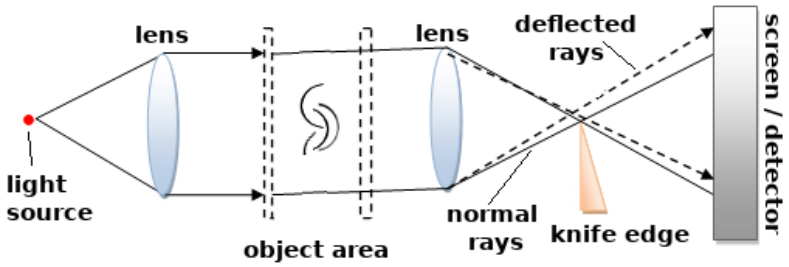

Figure 2.8: Sketch of a Schlieren imaging set-up. A point-like light source and a lens produce a parallel beam to illuminate the object. A second lens focusses the beam and produces an image on the screen or the detector. The knife-edge in between can be applied to cut off the non-deflected light rays. The figure is adapted from [Ind18a].

a spot. While the parallel rays ideally fall together at this point, the deflected rays are slightly shifted. This effectively broadens the focal spot. From the focal spot the beam propagates on to either a screen or a detector, where an image of the object is formed. The idea of Schlieren imaging is to block a part of the beam at the focal spot. When a knife-edge is inserted, for instance from below, to cover the focal spot, only the rays deflected above the spot reach the detector. Such a deflected ray is indicated in Figure 2.10. The horizontal knife-edge gives phase-contrast in the vertical direction. Thus, the detector receives light only from the positions, where a gradient in refractive index is present in the corresponding direction.

The description above is based on a perfect parallel beam. The set-up uses a point-like light source in the focal spot of a lens to produce a parallel beam. In a real set-up, the beam is not perfectly parallel due to the finite size of the source. Since the focal spot in the knife-edge plane is an image of the light source, it has a finite size as well.

Two important parameters of the Schlieren imaging system are the sensitivity and the measuring range. The sensitivity is influenced by the focal length of the second lens and the height of the light source $2a$, as illustrated in Figure 2.9. The horizontal shift of the light source image due to deflection at the Schlieren object is labeled with Δa. A shift upwards allows more light to be transmitted onto the screen. The corresponding point in the image of the object appears brighter. Analogously, a downward shift darkens the image. In contrast, Δb does not influence the intensity on the screen, since the amount of transmitted light remains unchanged. The displacement scales with the focal length f_2 and the diffraction in the medium δ by [Set01]

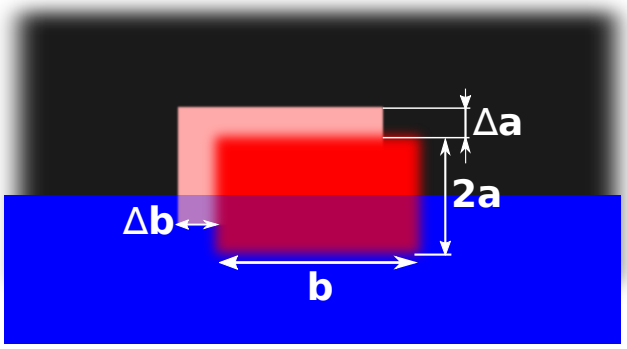

Figure 2.9: Illumination in the knife-edge plane. The rectangular source produces an image of size $2a \times b$ in the knife-edge plane (central red rectangle) which is partially blocked by the knife-edge (blue). The Schlieren object shifts the rectangle vertically by Δa and horizontally by Δb. The sketch is adapted from [Set01].

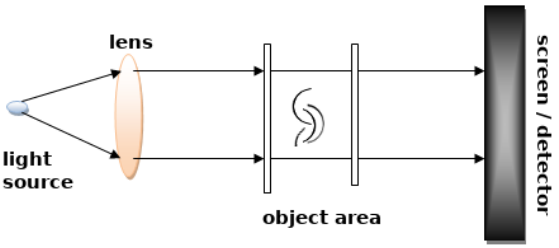

Figure 2.10: Sketch of a shadowgraphy set-up. A point-like light source and a lens produce a parallel beam to illuminate the object. A screen or detector is used to view the shadow that the object casts. The figure is adapted from [Ind18b].

$$\Delta a = f_2 \cdot \delta \,.$$

At $\Delta a = |a|$, the limit of the measuring range is reached. From that point on, the displaced source image is projected either completely on the knife-edge, or passes it without being cut. Consequently, the illumination of the detector does not depend on δ anymore. In conclusion, a longer focal length and a smaller size of the source increase the sensitivity [Cor68], whereas a high sensitivity reduces the measuring range of the system.

2.3.4 Optical Shadowgraphy

Optical shadowgraphy is a closely related approach to Schlieren imaging. The two main differences are the complexity of the set-up and the quantity that is measured. This section follows the discussion in [Set01].

Due to diffraction, transparent objects cast visible shadows which can be viewed on a screen as shadowgraph. As example, the shadowgraph of a plasma plume is shown in Figure 2.3. A shadowgraphy set-up can be seen in Figure 2.10. It is possible to use either a parallel or a cone beam. The object is magnified onto the detector or the screen in a cone beam set-up. For thicker objects, this can cause a distortion due to decreasing magnification along the optical axis, which can be circumvented with a parallel beam. A Schlieren object deflects a portion of the light beam away from its original path. Consequently the light arrives displaced at the screen. Intensity variations on the screen, which can be caused by the displaced light rays, manifest as increased brightness or as shadows on the screen. In contrast to Schlieren imaging, a shadowgraphy is not a focused optical image, but rather a shadow of the transparent object.

A Schlieren object with a constant refractive index gradient causes a uniform displacement of the light rays on the screen. A glass wedge is an example for such an object, if its boundaries are neglected. Since the rays are uniformly displaced, the intensity at the screen shows no variations. Hence, in contrast to Schlieren imaging which measures the first spatial derivative of the refractive index, shadowgraphy is only sensitive to the second spatial derivative of the refractive index.

2.3.5 Optics

Before describing the experimental methods in the next chapter, some theoretical concepts on the optical equipment employed in the experiments are introduced in this section.

Lens Equation

The lens equation describes the formation of an image by a thin lens of focal length f. The process is sketched in Figure 2.11. A detector sees a sharp image of an object if the geometry of the problem follows the thin lens equation given by [Hec14]

$$\frac{1}{f} = \frac{1}{d_o} + \frac{1}{d_i} \tag{2.18}$$

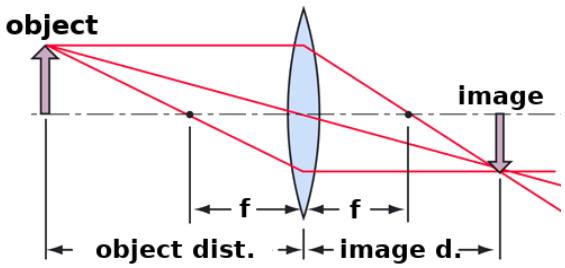

Figure 2.11: Image formation with a thin lens of focal length f. The object and the image are represented by arrows. The sketch is adapted from [Nav19].

where d_o is the distance between object and lens and d_i the distance between the lens and the image of the object. If the focal length and one of the distances, for instance the object distance, are known, the other distances, in this case the image distance, can be calculated from this equation. This is applied to experimentally determine the detector plane within the camera in Section 4.1.1.

Geometric Magnification

The concept of geometric magnification is present throughout all experiments. The light source S is assumed as ideal point and the beam as a cone that propagates to an object O and then to the detector D uniformly as straight rays. The distances are $d(S, O)$ from the source to the object and $d(S, D)$ from the source to the detector. The geometric magnification is defined as

$$M = \frac{d(S, D)}{d(S, O)} .$$

The intercept theorem states, that the magnification defined here is the same as the magnification that an image a in the object plane experiences when viewed in the object plane A, so that [Hec14]

$$\frac{A}{a} = \frac{d(S, D)}{d(S, O)} . \tag{2.19}$$

3 Methods

In this chapter, the different set-ups for the experiment are introduced and the hardware components as well as the software are described.

3.1 Introduction of the Set-Ups

The experimental set-up is placed on an optical table of 3 m length. Figure 3.1 shows the Talbot interferometer on the table with a light source, a grating and a camera. For imaging of test objects, they are placed between the laser and the grating. To minimize unwanted artifacts from in-line signatures in the grating-based reconstructions, the objects are positioned close to the grating. The laser beam is focused onto a spot that lies 12 cm away from the laser. Thereof, the beam propagates on in the shape of a cone beam. In the calculations, the focus is assumed as the light source. All test samples are placed in the divergent beam behind the focus spot, so the effect of geometric magnification is always present. But since the beam divergence is small, the magnification is negligible for objects in close proximity to each other.

The camera is mounted on a linear stage which allows positioning in z-direction with micrometer precision [New19a]. Controlled by the Software Matlab on the

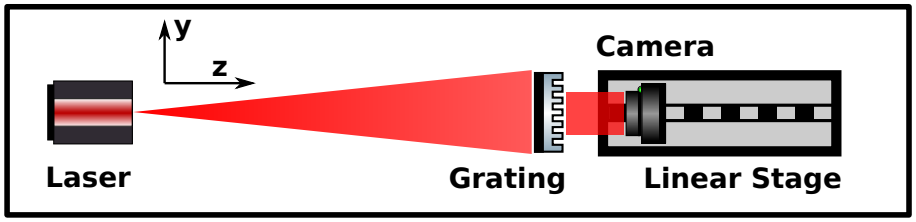

Figure 3.1: Sketch of the Talbot interferometer on the optical table as observed from above. The sketch is not in scale. The cone-beam of the laser fully illuminates the Talbot grating. After that, the modulated beam propagates on and is detected by the camera which is mounted on the linear stage. The test object would be placed in front of the grating.

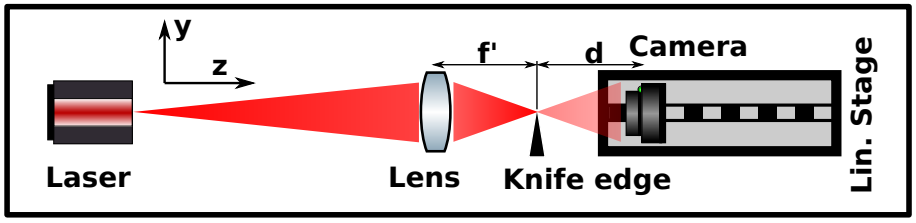

Figure 3.2: Sketch of the implementation of a Schlieren set-up. By the lens, the beam is focused into the knife-edge plane, where part of the beam is blocked so that it cannot reach the camera. Due to the divergence of the beam, the distance f′ between lens and focal spot deviates from the focal length f of the lens. The distance d between the knife-edge and the camera is marked accordingly.

laboratory computer, the stage can be moved over a range of 7.5 cm. The stage is utilized to measure the Talbot carpet. To that end, the camera is mounted on the stage and placed within the laser beam behind the grating. The intensity distribution at this position is measured and saved. After that, the camera is moved one step further away from the grating to measure the intensity at the new position. The procedure is automated with a Matlab script. If the Talbot distance is larger than the travel range of the stage, the procedure will only yield a section of the Talbot carpet.

The set-up in Figure 3.1 can be altered to test further phase-contrast imaging techniques. To implement shadowgraphy or an in-line phase contrast set-up, it is sufficient to simply remove the Talbot grating. For this, the object can be placed anywhere between the laser and the camera. So, the propagation distance from object to camera is a design parameter. The limitations on the parameter range are examined in the evaluation in Section 4.5.2.

In the approach of Schlieren imaging, a lens and a knife-edge are added as sketched in Figure 3.2. The Schlieren set-up described in Section 2.3.3 requires an additional lens to produce a parallel beam. But since the distance d_o between light source and lens is much larger than the focal length the beam is assumed approximately parallel and the additional lens is omitted. Every glass surface in the beam path causes unwanted signatures due to dust and dirt or scratches. By leaving out one of the lenses, this disturbance is reduced and the additional lens aberrations are avoided as well. The downside is the beam divergence that causes a small deviation between the nominal f and the effective f′ focal length of the lens. The deviation is derived from the lens equation to

$$\frac{\mathrm{f}'}{f} = \frac{d_o}{d_o - f} \approx 1 + \frac{f}{d_0},$$

where $f \ll d_0$ is assumed for the approximation of the equation. In the experiments, the lens is placed about 2 m from the source. The focal length of the lens is about 20 cm and the deviation remains at roughly 10 %. This is not found to cause any problems in the experiments, which is why the second lens is omitted.

3.2 Amplitude and Phase Gratings

The first challenge for setting up a Talbot interferometer is to find amplitude and phase gratings with suitable parameters.

The upper limit of the grating period is defined by the length of the optical table. Amplitude gratings produce a self image at the half Talbot distance, as mentioned in Section 2.3.1. For a grating with a period of up to 1.4 mm and a parallel red laser beam, this would fit on the 3 m optical table. The pixel size of the detector limits the grating period. The single shot Fourier imaging algorithm works reliably with 6.5 detector pixels per period or more [Gal17]. For the camera described in Section 3.3.1, this gives a lower limit on the period of 31.2 µm.

The experiments are conducted with amplitude gratings made out of photographic reversal films, which are known from slide projectors. Printed reversal films are commercially available [Dia18]. These 36 mm wide film stripes are offered with a resolution in the range of 120 to 160 lines per mm. Image files of black-and-white stripe patterns with different periods and widths are printed to such films and each mounted between acrylic glass plates to keep them from bending. A photograph of such a grating is shown on the right in Figure 3.3. The design parameters for the gratings can be found in Table 3.1. The fact that these gratings are inexpensive and immediately available for purchase is a great advantage over phase gratings.

In addition to the amplitude gratings, the experiments use a phase grating as well. It is shown in Figure 3.3 on the left. The picture reveals that the carrier plate has several scratches and a lot of dirt on it. The grating is borrowed from another work group, but no supplementary specifications are available. Thus, certain assumptions are made on the design parameters. As far as possible, these assumptions are validated experimentally in Section 4.3. From the marks on the plate, the grating period is assumed as 35 µm. The mark 'h=580' is assumed to refer to the depth of the grating structure in nanometers. The measurements presented in Section 4.3

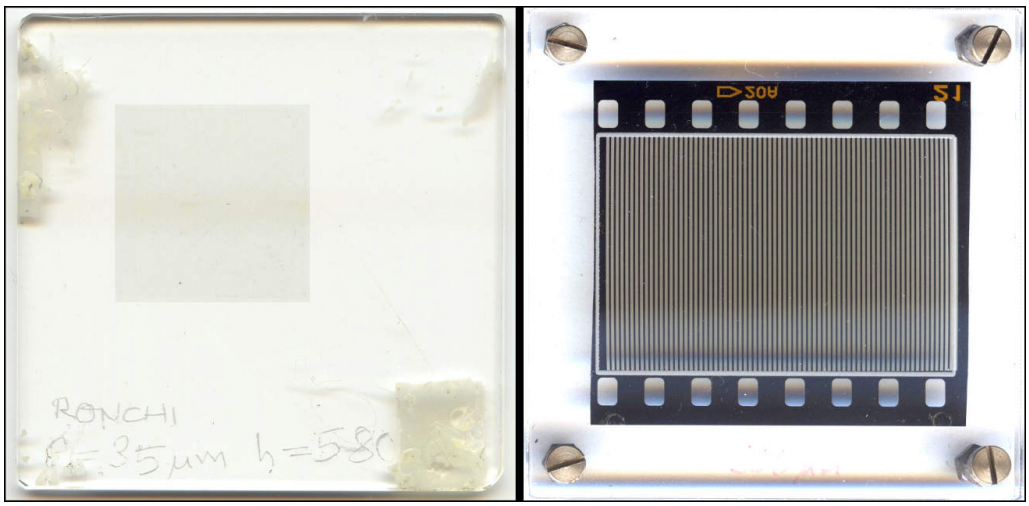

Figure 3.3: Picture of the 35 µm phase grating carrier plate (on the left) and the 500 µm absorption grating in its holder (on the right). The phase grating structure can be seen as an fant square on the upper left side of the carrier plate. The two lines of the inscription at the bottom read 'RONCHI' and 'P=35 µm h=580'. The absorpton grating is a cut-out photographic reversal film fixed with four screws between two acrylic glass plates. The inscription at the bottom reads '500 µm', but is hardly readable in the picture.

Table 3.1: Overview of the eight amplitude gratings and the phase grating. The design period is given for the gratings with different duty cycles. The Talbot distances Z_T and the first fractional Talbot order Z_H is calculated for an optical wavelength of 650 nm. For the phase grating, the duty cycle is unkown and the fractional Talbot orders cannot be calculated, since η depends on the phase depth, which is unkown as well.

Period [µm]	Modulation	Duty cycle	Z_T [mm]	Z_H [mm]
800	amplitude	1 / 2	$1.97{\cdot}10^3$	985
61.5	amplitude	1 / 2	11.64	5.82
35.2	amplitude	1 / 2	3.81	1.91
800	amplitude	2 / 3	$1{,}97{\cdot}10^3$	985
500	amplitude	3 / 5	769	385
200	amplitude	3 / 5	123	61.5
26.4	amplitude	1 / 3	2.14	1.07
26.4	amplitude	2 / 3	2.14	1.07
35.0	phase	–	3.77	–

suggest, that the gratings phase is neither $\pi/2$, nor π, but somewhere in between. The consequences for frequency doubling are discussed there as well. Since the period is the only reliable parameter for the phase grating, only this is given in Table 3.1 while the duty cycle and the fractional Talbot distances are omitted.

3.3 Components of the Set-Up

In addition to the gratings, further components are involved in the set-up which are introduced in this section.

3.3.1 Detector

The detector for the optical Talbot interferometer is a DMK 33GP5000e camera from the vendor The Imaging Source Europe GmbH. The sensor has 2592 x 2048 pixels. Each has a size of 4.8 µm. The monochrome detector is a CMOS sensor with a global shutter adjustable from 50 µs to 10 s exposure time. The details on the specifications can be found in Table 3.2. The camera is operated without photographic objective. Thus image plane is identical to the detector plane. The sensor is protected by a cover glass which causes interference patterns in the detected images [Bas19]. How to handle these fringes is addressed in Section 4.1.2.

The output signal of standard CMOS sensors behaves linearly to the incident light intensity, up to a certain limit [ASA+06]. Before reaching the maximum of the detector's intensity range, the output signal becomes non-linear [Sta08]. If not specified otherwise, the illumination is kept at half of the camera's dynamic range throughout the experiments to avoid this distortion. Another problem is that the

Table 3.2: Specifications of the camera used as detector [The18].

Name	DMK 33GP5000e
Resolution	2592 × 2048
Pixel size	4.8 µm
Sensor format	1 inch
Sensor type	CMOS
Shutter type	Global shutter
Exposure time	50 µs to 10 s
Gain	0 dB to 921 dB
Operating temperature	-5 °C to 45 °C

Table 3.3: Specifications of the laser module used as light source [Qua18].

Name	VLM-650-02 LPT
Operating Voltage	2.6 – 5.0 V
Operating Current	<35 mA
Output power	<1 mW
Wavelength at peak emission	(650 ± 5) nm
Focal length	10 cm – ∞
Safety class	3A
Beam Divergence	0.5 mRad

detector can show a signal different from zero even if the light source is off. An image taken with the light source off is referred to as offset image. A part of the spurious signal stems from the dark current of the CMOS sensor [Yor11]. But a significantly larger part is caused by the stray light background. Different light conditions in the laboratory cause different offset images. Prior to each series of measurements this offset is recorded. During the measurement the light conditions are kept constant, so that the background can be compensated for in the acquired images.

As is shown in Table 3.1, the finest gratings used in the experiments for this thesis have Talbot distances in the range of a view millimeters. To find these distances, it is important to know the position of the CMOS detector within the camera housing. From outside, this position is not obvious and there is no information about it in the specification sheet [The18]. As mentioned before, the sensor is protected by a cover glass. However, there is no information on how thick that glass is, or how much space is between the glass and the detector. Consequently, the detector plane within the camera must be identified experimentally, as is presented in Section 4.1.1.

3.3.2 Light Source

The light source used throughout all experiments is a red diode laser with rectangular beam profile [Qua18]. The specifications are given in Table 3.3. A built-in lens is mounted on the outlet of the laser module. With this, the focal length of the laser is adjustable within a certain range. The lower end of this range is specified with 10 cm. To avoid problems the laser is kept slightly above that value at 12 cm for all measurements. This maximizes the beam divergence which is necessary to fully illuminate the detector.

3.3.3 Test Object

For test measurements with the optical set-up, an object with known properties is needed for imaging. The future perspective of this work is the imaging of laser produced plasma which means that small dynamic samples are of interest, as discussed in Section 2.2.3. The approach to this is a jet of butane gas in ambient air.

The gas streams out from a 3D-printer nozzle, which is shown in Figure 3.4. Nozzles with 7 different inner diameters in the range from 0.2 mm to 1.0 mm are available for the measurements. The inner diameter of the 1.0 mm has been experimentally confirmed to lie in the range from 1.0 mm to 1.1 mm. The diameters of the other nozzles were not confirmed.

The gas is fed from a small gas bottle through a plastic tube to the lower end of the nozzle and streams out through the tip. The tip is visible as black shadow in some of the measurements. The gas streaming out from the tip of the nozzle is referred to as 'gas jet' in the following. The geometry of the jets is assumed as infinitely high cylinders originating from the nozzles. The jet diameters are assumed to be equal to the inner diameter of the nozzles. Problems caused by this rather rough approximation are discussed in the evaluation of the experiments. There are two butane isomers with different refractive indices. They are 1.00126362 for n-butane and 1.00126231 for iso-butane [WRD36]. Since the exact composition of the available gas in the experiments is unknown, a refractive index of 1.001263 is assumed, which corresponds to the average with less valid digits. The refractive index of ambient air at normal conditions is 1.000276 [Mik18], so that the relative refractive index can be given as Δn=987·10^{-6}. From this value, the phase-shift induced by the gas is estimated assuming a 0.1 mm thick cylinder of butane gas surrounded by ambient air. In the central region, the 650 nm laser beam traverses 0.1 mm gas with a relative refractive index of 987·10^{-6}. From Equation 2.6, this calculates to a phase-shift of 0.95 rad.

Figure 3.4: Picture of a 3D-printer nozzle with a 6 mm thread. The drill hole from bottom to the tip has an inner diameter of less than 1 mm. The image is taken from [Mic19].

3.4 Software

While Schlieren imaging and shadowgraphy are feasible in an analog set-up with a paper screen, the reconstruction algorithms for Fourier imaging and in-line phase-contrast depend on elaborate computational efforts.

As mentioned in Section 3.1, the linear stage is controlled with help of the computational environment Matlab to measure Talbot carpets. But more importantly, the simulation of such carpets is done implemented in Matlab as well. The full Talbot carpet is calculated from the grating's geometry, its material properties and from the properties of the incident light. The reconstruction for Fourier imaging is done with Matlab as well. A script is employed to calculate the three image modalities from the reference and object measurements. To that end, the properties of the grating, the wavelength of the light and the geometry of the set-up as well as the grating are required. The information required for the reconstruction of in-line phase-contrast images, that is done with a Matlab script as well, is described in Section 2.3.2.

As addressed in Section 4.4.1, noise can severely affect the application of such scripts. The unwrapping algorithm described in Section 2.3.1 is implemented as Matlab script. Especially in noisy images, it can occur that the program interprets random fluctuations between two successive pixels as phase wrap. Equivalently it occasionally fails to identify a jump in the image that is actually caused by phase wrapping. Since the algorithm is implemented line-wise in x-direction, unwrapping artifacts appear as horizontal lines that have an offset of approximately 2π to their surrounding in y-direction. If the object does not cover the whole image, so that the signal on both sides of the image is always within the range from $-\pi$ to π, this can be used for error correction. If the unwrapped signal at the boundaries deviates from the initial values, the algorithm must have misinterpreted at least one pixel in the line. So, the whole line is reevaluated with adapted parameters. However, if two errors

appear in one line they might cancel each other which cannot be corrected this way. The influence of unwrapping artifacts is regarded in Section 4.4.1.

The camera is controlled by the software tool IC Capture. The program is utilized to adjust parameters like the exposure time or the gain, though the latter is always set to the lowest level. Further, the camera images are read out and displayed in live view with IC Capture. Furthermore, the program can record and save image sequences with adjustable timing. If a high frame rate is required, the camera pixels can be binned to reduce the transmitted data rate. Alternatively, the part of the sensor that is read out can be limited as well.

4 Experiments and Analysis

The goal of the experiments is to apply the phase-contrast imaging techniques for imaging of a test sample, which is a butane gas jet. To that end, the components of the three set-ups are characterized before they are compared to each other by conducting phase-contrast measurements. Phase-contrast imaging is motivated in Section 2.2.1 for its capability to determine refractive index of a transparent medium. In a plasma, this is equivalent to the determination of the electron density. The refractive index is proportional to the phase-shift measured along the line of sight. However, as discussed in Section 3.3.3, the relation between the refractive index and the thickness of the jet is assumed to be constant. This allows, to represent the measured phase-shift in terms of the thickness of the butane gas jet, which is a more demonstrative quantity when comparing it to the diameter of the nozzles.

4.1 Characterization of the Camera

Before testing the imaging set-ups, the components are characterized individually. This is done for the camera first.

4.1.1 Position of the Detector Plane

As discussed in Section 2.3.5, the position of the detector plane within the camera is not obvious from outside. But it can be determined with the lens equation introduced in Section 2.3.5. The idea is to use a lens of known focal length and image an object that is placed at a certain distance from the lens. With the camera placed behind the lens the system is manually aligned to obtain a sharp image of the object. In this configuration, the distance between lens and CMOS sensor is given by the lens equation. Thus, the position of the detector in the camera housing is obtained independently of prior knowledge on the cover glass or other components.

The object is a flat piece of cardboard with markings printed on it. It is standing upright at a distance of d_o=214.0 cm from the camera. It is illuminated with an ordinary desk lamp. A lens is placed on the optical axis between the object and

the camera. It has a focal length of $f = 106.0\,\text{mm}$ and is moved slowly away from the camera towards the object, until a sharp image of the object can be seen on the detector. The distance between the lens and the front of the camera housing, at which a sharp image is obtained, is $\tilde{d}_i = (104 \pm 0.5)\,\text{mm}$. To calculate the distance d_i from the lens to the detector at which a sharp image is obtained, Equation 2.18 is converted to get

$$d_i = \left(\frac{1}{f} - \frac{1}{d_o}\right)^{-1} .$$

With the geometry described above, this calculates to $d_i = (111.5 \pm 0.05)\,\text{mm}$. So, the distance from the front edge of the camera housing to the detector is $d_i - \tilde{d}_i = (7.5 \pm 0.6)\,\text{mm}$. Therewith, the geometry of the camera is better understood, which is important to accurately align the optical set-up.

4.1.2 Thin-Film Interference

Thin-film interference between the CMOS sensor and the cover glass of the camera can be the cause of an unwanted interference pattern [Bas19]. An example for such patterns is shown in Figure 4.1. If the shape of the pattern changes over time, it appears differently in the reference and the object images and thus cannot be completely removed from the data. This can lead to artifacts in the reconstructed images.

To quantify the change of the patterns over time, a series of reference is recorded over a long period of time. To that end, the laser is directly illuminating the camera without a grating or a sample in the beam path. Prior to data taking, the laser is already warmed up for one hour, to ensure that it has reached a steady operating temperature. Then, for a time period of three hours the camera records one image every 20 seconds. The exposure time is adjusted such, that the average intensity of the image is roughly in the center of the camera's dynamic range.

From the resulting sequence, each image is divided pixelwise by the previous one. For every image, this gives a map of quotients from which the mean value and the standard deviation can be calculated over all pixels of the map. This is done for all images of the sequence and the result is plotted in Figure 4.2. Within the first 30 minutes the mean declines, which means the change between the patterns becomes smaller. After 30 minutes, the mean and the standard deviation fluctuate around a steady value. That the steady value is not zero is most likely due to the noise in each image. Interestingly, before reaching its steady value, the standard deviation

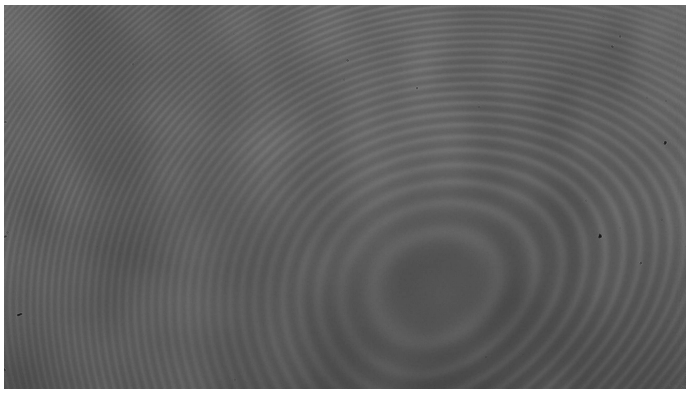

Figure 4.1: Typical gray scale reference image taken with the camera under illumination by the laser and a completely free beam path. Two distinct patterns are visible. An approximately ring-shaped pattern caused by thin-film interference and the larger pattern that can be faintly seen in the upper half of the image. It has a much larger period and consists of only 8 fringes over the whole width of the image. It stems from the intensity distribution in the laser beam profile.

is even slightly smaller. A possible explanation for that would be that the change between the subsequent images has a certain systematic behavior during that time. The changes of the interference pattern could be caused by a mechanical expansion in the camera due to its operating temperature.

To conclude, the unwanted change in signal due to thin-film interference becomes less severe with time. For that reason, the camera is warmed up for about 30 minutes prior to data taking. But even then, the artifacts caused by these patterns cannot be fully suppressed.

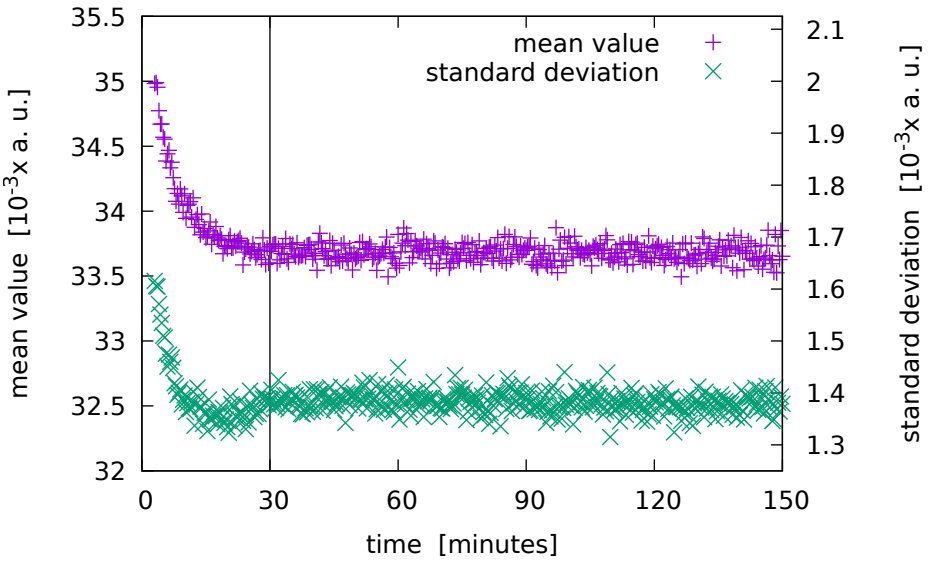

Figure 4.2: Change of the measured intensity between two consecutive images. The quotient is calculated for every pixel independently. Plotted are the mean value and the standard deviation over all pixels. A vertical line is placed at 30 minutes which is defined as the warm-up time of the camera.

4.2 Characterization of the Amplitude Gratings

To characterize amplitude gratings, the design parameters are experimentally verified and the visibility of the Talbot pattern is determined. As a first step, the Talbot distances are confirmed by analyzing the shape of the Talbot pattern.

4.2.1 Determination of the Talbot Distance

To find the Talbot distance of the absorption grating with a 200 µm period, the Talbot carpet was measured and compared to the simulation. Both carpets are plotted in Figure 4.3. The z-range of the measurement is limited by the size of the linear stage. The y-range is cropped for clarity, so that the Talbot pattern corresponding to 3 grating bars is visible. An equivalent of this range was simulated as described in Section 3.4. An obvious difference between simulation and experiment is the slope in y-direction of the measured carpet. The slope is caused by a small misalignment of the linear stage. The axis along which the stage moves is tilted by less than 2° in respect to the optical axis of the laser beam.

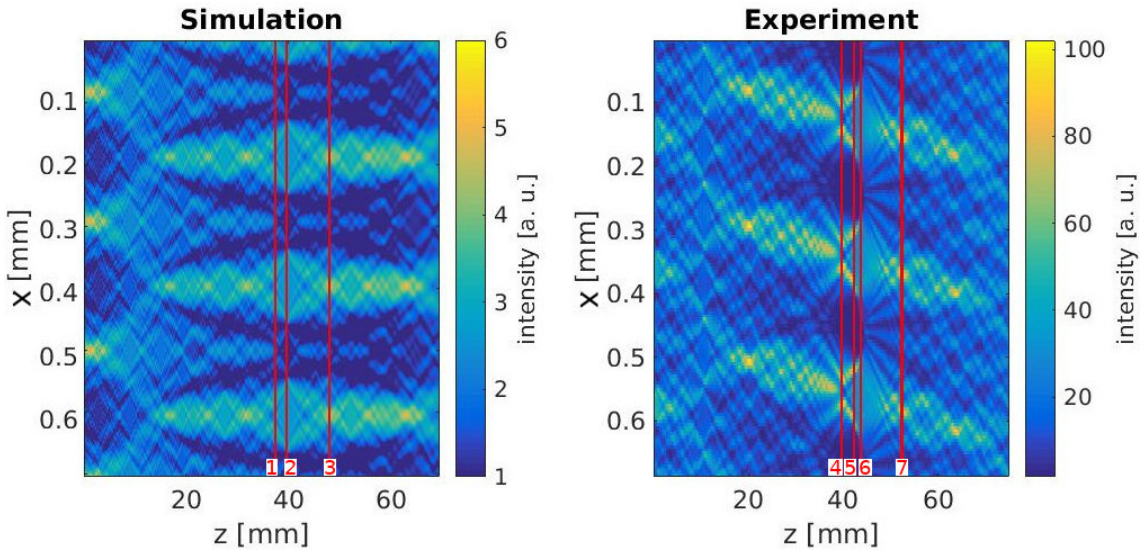

Figure 4.3: Extract of the Talbot carpet of the 200 µm amplitude grating obtained by simulation (on the left) and by measurement in the experiment (on the right). The grating is placed in the x-y plane, the detector moves in z-direction. The numbered red lines, mark the positions of the line plots LP 1 to LP 7 in the Figures 4.4 and 4.5.

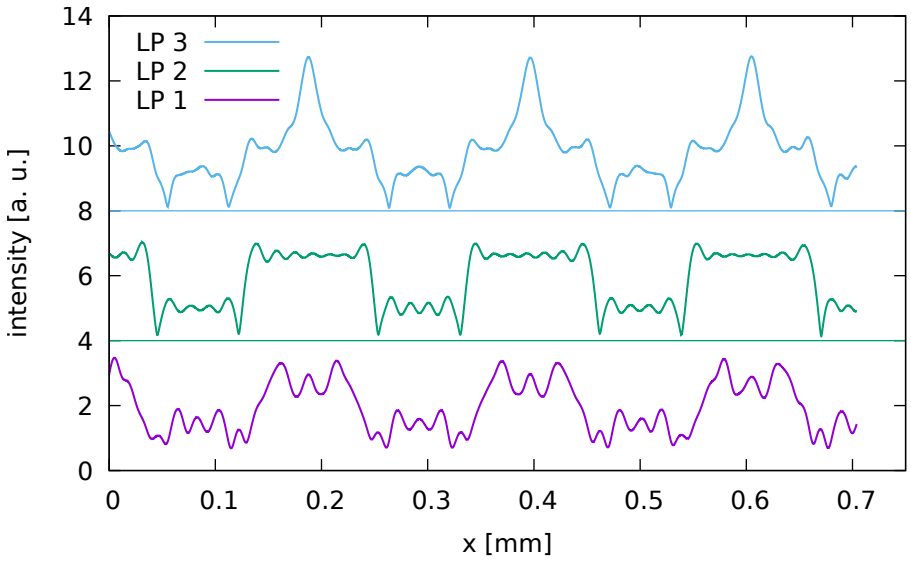

Figure 4.4: The intensity profiles for the three lines (LP 1, LP 2 and LP 3) that are marked in the simulated data in Figure 4.3. As marked by the two horizontal lines in this plot, the profiles are separated in the vertical direction for more clarity.

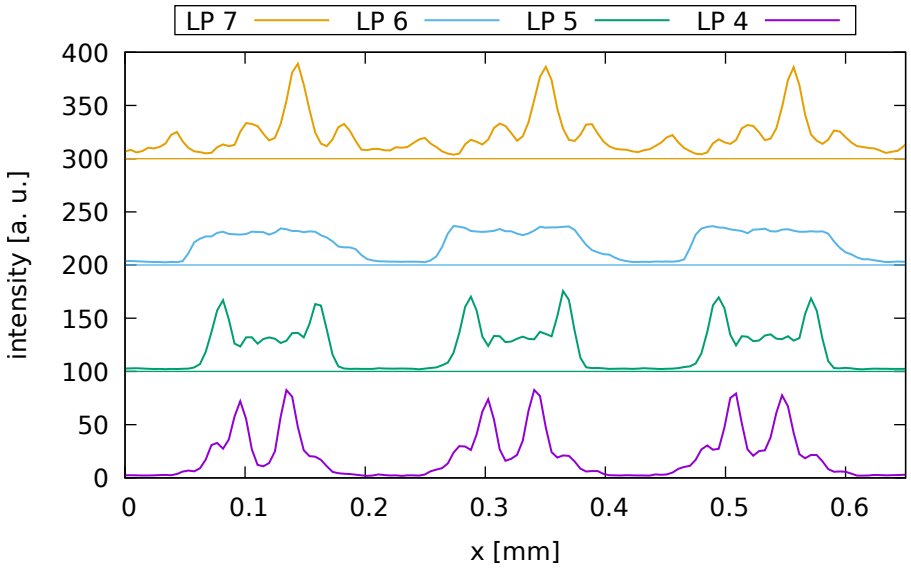

Figure 4.5: Intensity profiles for the four line plots LP 4, LP 5, LP 6 and LP 7 that are marked in the simulated data in Figure 4.3.

From the measured Talbot carpet, four distinctive line plots were extracted and plotted in Figure 4.5 with the numbers 4-7. The line plot LP 4 is chosen such, that the point of highest intensity is captured. It exhibits two peaks. LP 7 is the line with the highest peak intensity that exhibits only one peak. LP 5 reproduces the binary structure of grating bars and slits, except for a small peak at every junction. And finally, LP 6 is chosen similarly to LP 5, except that the boundaries of the bars are smooth and exhibit no peaks.

Additionally, three line plots were extracted from the simulated carpet at analogous positions. They are numbered 1-3 and plotted in Figure 4.4. The line plot LP 2 is situated exactly at the calculated Talbot distance Z_T, which lies between LP 1 and LP 3. The equivalent of LP 4 with its multiple high-intensity peaks is LP 1 from the simulation. It lies at a shorter distance than Z_T. The equivalent of LP 7 was found behind Z_T and is labeled LP 3. In contrast to the initial expectation, LP 2 does not look like the line plots measured at the high-intensity positions, but rather like LP 6 in between, when judging from the sharp boundaries between grating bar and gap.

For the 200 µm grating, the position of the first half Talbot distance Z_H^1 was measured at (63.1 ± 0.2) mm behind the grating. To compare this to the design value from Table 3.1, the measured values must be corrected for the magnification by Equation 2.19. The distance from source to detector is 235 cm and from source to grating it is 229 cm. With this, Z_H^1 without magnification can be calculated to

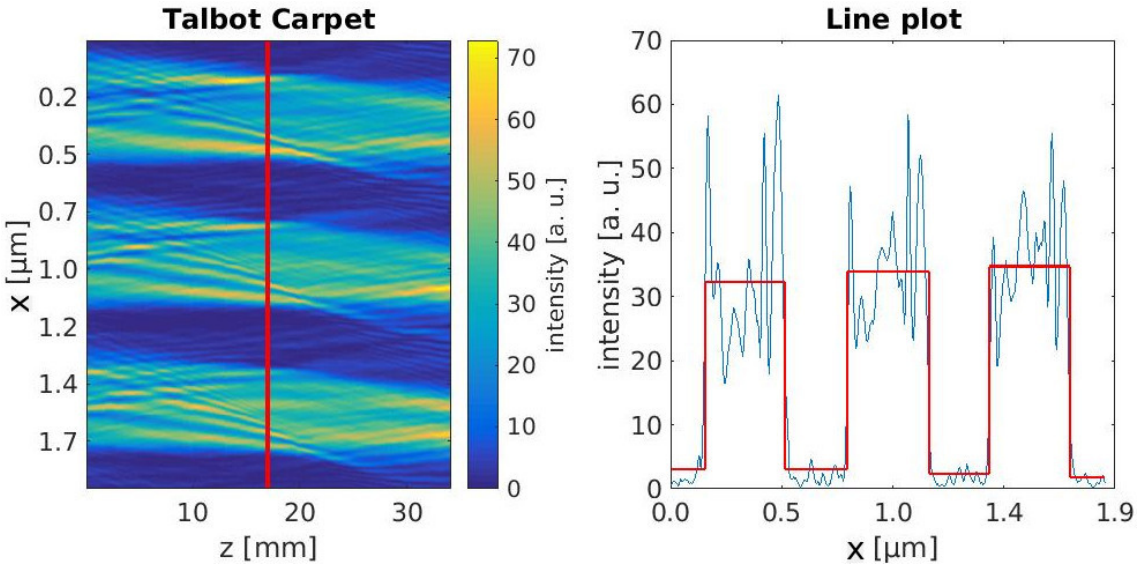

Figure 4.6: Measured Talbot carpet of the 500 µm grating (on the left) with a red line marking the z-position of the line plot (which can be seen on the right). The red profile in the line plot marks the boundaries and the mean intensities of the grating bars and gaps in arbitrary units. Due to a geometric magnification of about 23 %, the Talbot pattern shows a periodicity of 614 µm.

$Z_H^1 = (61.5 \pm 0.2)$ mm, which perfectly fits the expectation from Table 3.1.

In conclusion, a good agreement between experiment and theoretic expectation can be achieved for determining the Talbot distance from the Talbot carped, when looking into the overall shape of the line plots rather than just judging from the position of maximum intensity. After finding Z_T, the relevant parameters can be measured as described in the following section on the example of the 500 µm grating.

4.2.2 Visibility and Duty Cycle

To determine the visibility and to check the duty cycle of the 500 µm grating, the Talbot carpet was measured. Since, with 76.9 cm, the Talbot distance is about ten times as large as the travel range of the linear stage, a full Talbot carpet cannot be recorded. So, only a section around the assumed position of the first half Talbot distance Z_H^1 is measured. From this carpet, a line plot with sharp boundaries between the grating bars and gaps is extracted, associated with Z_H^1 and shown in Figure 4.6. The mean intensities of the plateaus and the gaps are marked in the plot. From their values the visibility is calculated to an average of (86±1) %. Since the variations within the plateau is systematic, it is not regarded in the determination

Table 4.1: Parameters of the amplitude gratings. The design period P is given together with the distance at which the parameter values were measured. The Talbot order N_Z is 0.5 if the distance equals Z_H^1 and else gives the Talbot order at which the parameters were measured. Visibility and duty cycle DC are given with their errors. The 800 µm and 26.4 µm gratings appear each with two different duty cycles.

P [µm]	Value at [cm]	N_Z	Visibility [%]	DC [%]
800	98.3 ± 1.0	0.5	86.5 ± 1	54.5 ± 1.3
800	98.3 ± 1.0	0.5	84.5 ± 4.8	60.4 ± 2.3
500	37.7 ± 0.02	0.5	85.9 ± 0.9	43.0 ± 0.8
200	6.14 ± 0.02	0.5	79 ± 1	48.8 ± 1.2
61.5	4.56 ± 0.02	4	67 ± 4	50.0 ± 2.0
26.4	4.36 ± 0.02	20	30 ± 8	33.0 ± 33
26.4	4.33 ± 0.02	20	6 ± 4	55.0 ± 38

of the error. The error is calculated from the variation of the three plateau values. The boundaries of the plateaus and gaps are marked as well. With them, the duty cycle calculates to (43±0.8) %, which deviates from the design value 40.4 %. A size deviation in the width of the grating bars of about 13 µm would be enough to cause this deviation. The resolution of the device that printed the amplitude gratings is given by the manufacturer with at least 8.3 µm. It is possible, that this plays a role in the deviation of the duty cycle from the design value, since both uncertainties are on the same scale of size.

The measured parameters of the amplitude gratings can be found in Table 4.1. They have been obtained by above described procedure of recording the Talbot carpet, finding the Talbot distance and calculating the parameters from the line plot. The results clearly show, that a higher visibility is achievable by using larger grating periods. This seems plausible, since larger periods mean lower requirements to the equipment and more camera pixels per grating period, which improves the sampling of the Talbot pattern. The error margin on the duty cycle becomes larger for smaller periods, because the width of the grating bars approaches the scale of the detector pixel size. The parameters were not measured at the same distance and not at the same Talbot distance. This is due to the experimental feasibility. The gratings with large periods were characterized at the first half Talbot distance. The others at higher full Talbot orders.

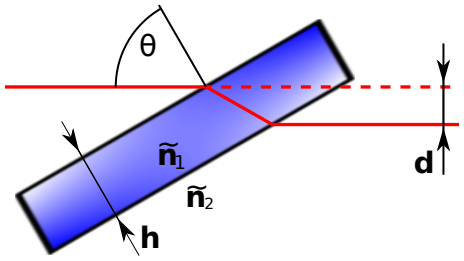

Figure 4.7: The laser beam (red) is incident on the phase grating plate with refractive index $\tilde{n}_1$ at an angle of θ. The refractive index of the surrounding medium is $\tilde{n}_2$. It is displaced in the plate of thickness h and propagates on parallel to its incidence. Sketch adapted from [New19b].

4.3 Characterization of the Phase-Grating

4.3.1 Refractive Index

Alongside the amplitude gratings, the experiments were also conducted with a phase grating. Unfortunately, the characterization is more complicated. The phase grating is borrowed from another work group and there are no supplementary specifications available. The only source of information is the inscription on the plate itself. The refractive index of the material is not given and the available specifications are, to a certain extent, open to interpretation as can be seen in Figure 3.3. Hence, these specifications are subject of the experiments.

The refractive index of the phase grating can be measured using a geometric set-up which is sketched in Figure 4.7. A laser of wavelength $\lambda = 650\,\text{nm}$ is used to irradiate a slit aperture. Laser and aperture are positioned with a distance, so that the incident light can be viewed as a parallel beam. The plate downstream the aperture is mounted such, that it can be rotated. The plate, rotated at an angle θ displaces the beam by $d(\theta)$. However, the direction of propagation is not affected. The displacement after the plate of thickness $h = (1.7 \pm 0.05)\,\text{mm}$ can be given as [New19b]

$$d(\theta) = h \sin(\theta) \left[1 - \frac{\cos(\theta)}{((n_2/n_1)^2 - \sin^2(\theta))^{0.5}} \right] , \tag{4.1}$$

where n_1 is the refractive index of air, which will be approximated to $n_1 = 1$ and n_2 is the refractive index of the plate. Since the plate is only 1.7 mm thick, the beam displacement is expected to be on the sub-millimeter scale. Thus, the CCD camera

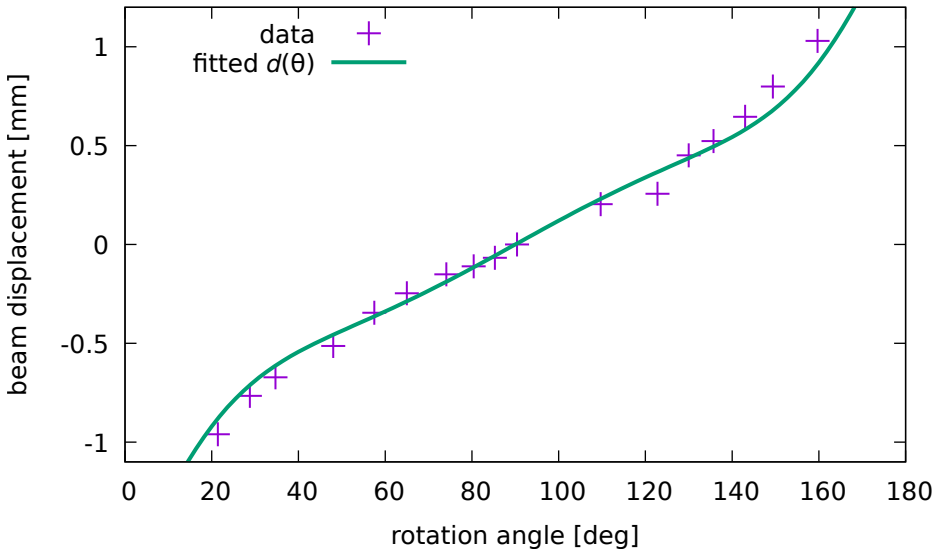

Figure 4.8: Beam displacement after the plate in µm is plotted over the plate's rotation angle θ. The expected beam displacement is fitted to the data with the plate's refractive index as fit parameter.

is used as to detect the displacement with high accuracy. The measured data can be seen in Figure 4.8. The fit function for the data is adapted from Equation 4.1 with n_2 as fit parameter. The result is $n_2 = (1.33 \pm 0.02)$ for the refractive index of the phase grating. The largest source of error is h, so the error margin on the refractive index is calculated from the uncertainty of h while neglecting the errors on θ and on $d(\theta)$. This is clearly smaller than the values given for glasses in [Mik18]. Seemingly, the plate is not made of glass. However, there are polymers with refractive indices around 1.3 to 1.4 [Omn18]. So, the value measured for the plate of the phase grating would fit into the region covered by polymers.

The plate's mass density can be used to support the result, that it is made of a polymer instead of glass. The density is $(1.93 \pm 0.03)\,\mathrm{g/cm^3}$. Fused silica, the glass given with the lowest refractive index in [Mik18] is given with a mass density of $2.2\,\mathrm{g/cm^3}$ in [Acc13]. Polymers, however, can be found abundantly in [Sci13] with densities ranging from $0.830\,\mathrm{g/cm^3}$ to $2.15\,\mathrm{g/cm^3}$ containing the value of the phase grating's plate.

4.3.2 Grating Period

The period of the phase grating is specified on the plate as 35 µm. To experimentally verify this specification, the far field diffraction pattern of the grating is analyzed with help of Equation 2.14 to calculate the grating period. The experimental set-up is implemented according to the description in the theory chapter and the sketch in Figure 2.4. A slit aperture is added to the set-up to limit the beam size and thereby increase the precision of the measurement analogously to the measurement described in Section 4.3.1. The grating is illuminated by the beam coming from the aperture. The laser beam is split into multiple beams in accordance with Equation 2.14. The beams finally impinge on the screen, where their separation distance can be measured. From this the diffraction angle α between the diffraction orders $m = +1$ and $m = -1$ is determined. For better statistics, the measurement is repeated at several distances between the grating and the screen. A total of 14 data points between 19.3 cm and 70.3 cm are recorded. The data points average to an angle of $\alpha = 1.064° \pm 0.007°$, which translates to a grating period of $(35.0 \pm 0.3)\,\mu$m. The specified period of 35 µm is therefore regarded as validated.

4.3.3 Phase Depth

The phase depth of a grating depends on the refractive index of its material, the wavelength of the scattered light and the height of the grating bars, as is described by Equation 2.15 in Section 2.3.1. On the plate of the phase grating, an inscription states $h = 580$. This could refer to the height of the bars in nanometers, but the meaning is not stated clearly. Thus, the grating's Talbot carpet, as determined by measurement, is compared to carpets calculated by a simulation with different optical phase depths. While this might give an insight to the gratings phase depth, it is more of a qualitative study than a quantitative examination, since the patterns tend to be ambiguous.

The procedure of measuring the Talbot carpets is, as described in Section 3.1, automatized to a certain degree. The grating and the linear stage with the camera on top are aligned in the laser beam path. The stage must be carefully aligned to be as parallel to the beam as possible, because with the large ratio between the size of the grating periods and the size of their Talbot distances even a small deviation from the beam path becomes visible, as already discussed in Section 4.2.1.

The carpet measured with this set-up is shown in Figure 4.9, alongside the simulated ones. The two ideal cases of a π- and a $\pi/2$-shifting gratings are plotted in the two upper subfigures. They are simulated in a parallel beam with an ideal non-absorbing phase grating and a high spatial resolution. A third carpet is simulated with a lower

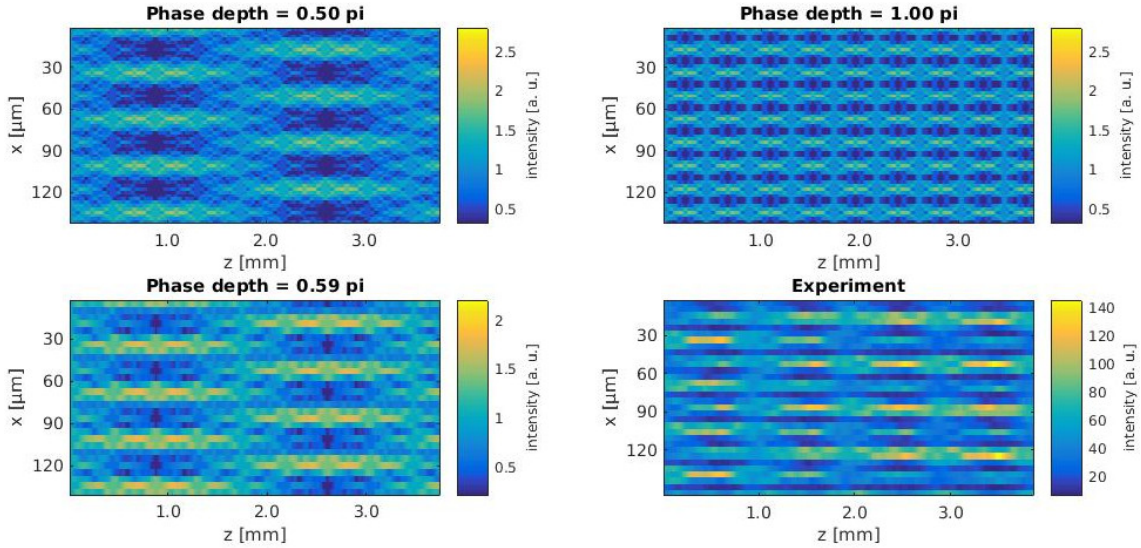

Figure 4.9: Three simulated Talbot carpets of the 35 µm phase grating and the experimentally measured one. The carpets simulated with phase depths of $\pi/2$, π represent the cases without and with frequency doubling. The simulated 0.59π carpet represents the assumed phase depth of the grating utilized in the experiments. By binning the pixels, it is adapted to the limited spatial resolution of the experiment. Also, the 0.59π carpet's range of the color bar is adapted to the experiment. The carpet labeled 'Experiment' is taken from a measurement starting from the fourth Talbot distance in a non-magnifying set-up. All simulations are conducted with a duty cycle of 0.5.

resolution, that corresponds to the experimental conditions set by the pixel density of the detector and the precision of the linear stage in z-direction. Also, the phase depth is adapted to resemble the real phase grating from the experiment. Assuming the measured refractive index $n = 1.33$ with a grating depth of 580 nm and using Equation 2.15, the optical depth of the phase grating for the 650 nm laser calculates to $\Delta\Phi = 0.589\pi$. Multiple carpets were simulated for different phase depths between π and a $\pi/2$. However, no suited criterion was found to judge the similarity between the simulated and the measured carpets. Subjectively, the simulation at $\Delta\Phi = 0.59\pi$ presented in Figure 4.9 suited the experimental carpet best, since the structure of the $\pi/2$ carpet is still clearly visible while frequency doubling can be observed as well. Nevertheless, finding an objective criterion for the similarity of two carpets would be necessary for a significant statement on the phase depth of the grating. The result could be further improved by repeating the measurements with different laser wavelengths or by using geometric magnification for better sampling of the intensity pattern with the given camera pixel density.

4.4 Talbot Imaging

After characterizing the camera and the gratings, test objects are measured to evaluate and compare the different imaging techniques. The ability to correctly measure the phase-shift induced by a sample can be tested quantitatively, if the geometry and the refractive index of the sample are known. The assumed values for the butane gas jets are introduced in Section 3.3.3.

4.4.1 Data Taking and Reconstruction

Before beginning with the evaluation, the procedure of data taking and reconstruction is outlined in this section for three example data sets picked from different measurements.

To retrieve the transmission, the phase-shift and the dark-field with the grating-based approach, an image sequence of the gas jet is recorded with the interferometer. The grating is aligned such that the grating bars are vertical to achieve sensitivity to the phase-contrast in the horizontal direction. After starting the sequence, a few frames are taken which serve as reference image. The sequence keeps running while the gas is fed to the nozzle forming a gas jet. These are the object images. For a measurement with the 61 µm amplitude grating, the reference and the object image can be seen in Figure 4.10. From these, the three image modalities are reconstructed.

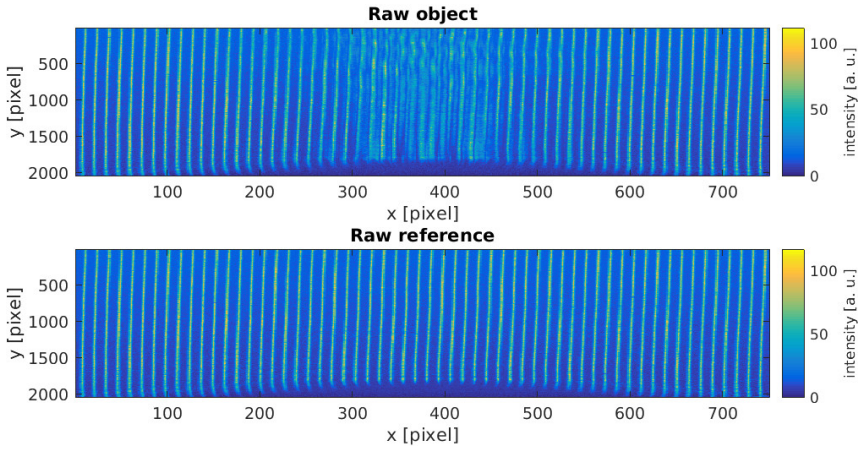

Figure 4.10: Raw images of the reference frame and the butane gas object for the amplitude grating and the 0.6 mm nozzle. The color code represents the light intensity detected by the camera. The grating's Talbot pattern is clearly visible in both images. The dark area at the bottom of the frames is the shadow of the nozzle. It appears distorted because the x range is cropped to the central region. In the object image, the jet is visible in the region above the nozzle.

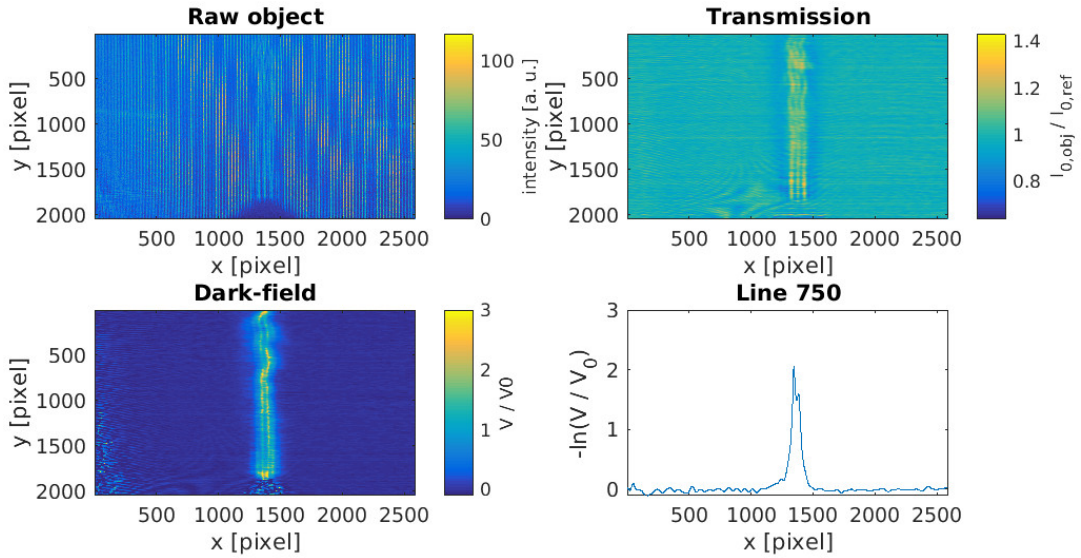

Figure 4.11: The raw object, the transmission and the dark-field image measured for the 0.6 mm nozzle with the 61 µm amplitude grating. The fourth subfigure shows a line plot through line 750 of the dark-field image.

The amount of light that is transmitted through the object is plotted in Figure 4.11 in the top right. The transmission in the object image relative to the reference is coded in color. Over large pars of the jet this relation is larger than one, which means that in those regions the amount of light detected is larger with object than without. However, this is not due to light amplification in the butane. The average transmission value of all pixels is 0.9872 with a standard deviation of 0.0115, which cannot be explained by an overall increase of the signal. The light is shifted locally within the image due to deflection and propagation. The artifacts appear as strips along the gas jet, which shows that intensity is shifted in the direction of the gradient of the refractive index. These propagation effects are not regarded in the grating-based reconstruction algorithms, causing these artifacts in the transmission image.

Also displayed in Figure 4.11 is the dark-field image of the gas jet. The outlines of the gas are clearly visible. Similarly to the transmission image, stripes along the jet can be seen in the dark-field as well. Away from the jet, the image has a nearly uniform background with a dark-field signal fluctuating around zero. Noise can be seen at the origin of the jet, where the nozzle extends into the image and on the left side of the image. The nozzle appears as shadow in both, reference and object image. If the reconstruction algorithm sees any visibility in that area. This is purely due to noise and the resulting values are small random numbers. So, in that area, the dark-field is a map of small numbers divided by each other. Thus, these small variations are translated to large values in the image. The noise on the left side of the image might be caused by varying stray light conditions during the experiment. The gas supply for the jet is manually controlled a few centimeters from the beam path to the left, so there is some movement that might change the distribution of background light. One representative line of the dark-field image has been plotted in Figure 4.11 as well. The gas jet is clearly visible as a high peak in the center of the plot. A dark-field signal of 1.6 roughly corresponds to a reduction of the visibility to a fifth of the initial value.

As motivated in Section 2.2.2, the phase-shift induced by the sample is highly relevant in potential astrophysical applications, because it directly relates to the electron density. From reference and object measurement, the reconstruction algorithm extracts the differential phase-shift as shown in Figure 4.12 on the top left for the example of a jet from a nozzle with 1.0 mm inner diameter that has been measured with the 35 µm phase grating. The differential phase-shift is proportional to the gradient of the refractive index which means that a large change of the index on small length scale causes a high signal, which can only be retrieved modulo to a factor of 2π, as discussed in Section 2.3.1. Consequently, the retrieved image exhibits multiple phase wraps which appear as hard borders in the color coded image between the differential phase-contrast values $-\pi$ and π. With the Matlab script described in Section 3.4, the image can be unwrapped. The resulting image, that is

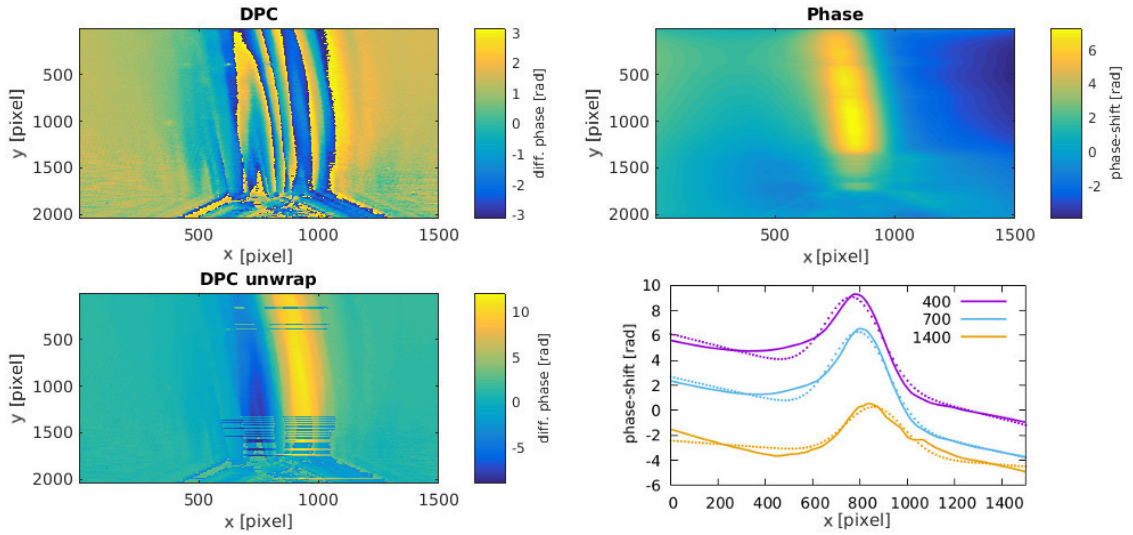

Figure 4.12: Images of the differential phase-contrast (DPC), unwrapped DPC (DPC_{unwrap}) and the line-integrated phase-shift (Phase). The fourth subfigure shows three line plots taken from the phase-shift image. Each plot is averaged over 50 lines, starting at the indicated lines 400, 700 and 1400. They are fitted by Gaussian functions (dotted lines) with linear offsets accounting for the background signal.

plotted in Figure 4.12, clearly shows the gas jet in the center. The horizontal lines in the image are unwrapping artifacts. As discussed in Section 3.4, the unwrapping algorithm sometimes partially shifts a line wrongly up or down. The consequences of these errors are discussed in the next paragraph. Another issue is the sign of the differential phase-contrast. The direction of the differential in the image is from left to right. At the left boundary of the gas, the refractive index integrated over the line-of-sight increases due to a rising gas density. The reconstructed differential phase-contrast takes negative values in that area.

Plotted in the top right of Figure 4.12 is the phase-shift. As discussed in the theory chapter, the phase-shift induced by the sample can be obtained from the differential phase-shift by integration. The sign for the integration is defined such, that a higher phase-shift actually refers to a region of a higher refractive index. While the outlines of the jet are visible in the image, the phase-shift and thereby either the density or the refractive index of the material seems to vary along the direction of the jet. There are multiple possible explanations for this. The exact dynamics of the jet are unknown. It is possible, that the velocity of the gas decreases after leaving the nozzle, which would either cause a higher gas density or a larger transverse extend of the jet. Both would increase the measured phase-shift signal. The pressure at the gas bottle fluctuates during the whole process of imaging, but whether the fluctuations happen on a time scale that is caught in a single frame does not lie within the scope

of the experiment. However, the phase-shift appears maximal where the differential phase-contrast shows no unwrapping artifacts. If a phase wrap is not correctly recognized, the magnitude of the signal is reduced by 2π. This deviation becomes more severe when it is integrated over the whole line. Thus, it seems likely, that the phase-shift appears with reduced values if the unwrapping algorithm breaks down.

To visualize this variation more clearly, three line plots were taken from the phase-image. Each of the three line plots is averaged over 50 lines, starting at the lines 400, 700 and 1400. The plot in Figure 4.12 shows them each with a Gaussian fitting curve. A linear offset is added to the Gaussians to account for the linearly decreasing background signal. There is a constant, in this case negative, offset present in the differential phase-shift. This uniform offset can be due to a slight movement of the grating caused for example by a vibration of the set-up. The constant offset is integrated in the phase and thus appears as a linear gradient throughout the whole image. The plot averaging the lines 700 to 750 is taken in a region without wrapping artifacts. Due to its asymmetric shape is not ideally described by the Gaussian function, but the fit converges. The amplitude of the Gaussian fit for the line plot 700 results as (7.0 ± 0.1) rad. The region with the strongest unwrapping artifacts is captured in the line plot 1400. The deviations are strong enough to cause a jump in the background signal. This is why the linear offset in the fit function cannot capture the background anymore and strongly deviates from the signal, as can be best seen in the region of small y-values. With an amplitude of (3.9 ± 0.1) rad, the fit returns a value for the phase-shift that is almost reduced by half of the value without unwrapping artifacts. In the upper region of the image, the line plot 400 yields only a slightly reduced amplitude with (6.7 ± 0.1) rad. This shows, however, that even a few artifacts can falsify the result of the evaluation.

Cylindrical symmetry is assumed for the butane gas jet, so the width seen in the image is assumed to correspond to the thickness along the optical axis. The width of the jet is defined with the $1/e^2$ criterion which means that the outer boundary of the jet is defined at the points, where the phase-shift has reduced to about 13.5 % of the maximum value. The object position during the above presented measurement causes a geometric magnification of 1.05. The magnified width of the Gaussian fit to the lines 700-750 corresponds to a jet diameter of (650 ± 5) µm. The corresponding nozzle has a diameter of 1.0 mm, which gives rise to the assumption that the size of the gas jet cannot simply be assumed to be the same as the inner diameter of the nozzle. This will be further addressed in Section 4.4.2. However, the phase-shift along the line of sight, that is calculated from the same line plot gives a thickness of (0.74 ± 0.01) mm, which is much smaller the nozzle diameter but larger than the thickness of the jet implied by the width of the Gaussian. Possible explanations for that are manifold. A decreasing gas temperature due to decompression after the nozzle could reduce the refractive index. Or the gas mixes with air in the outer

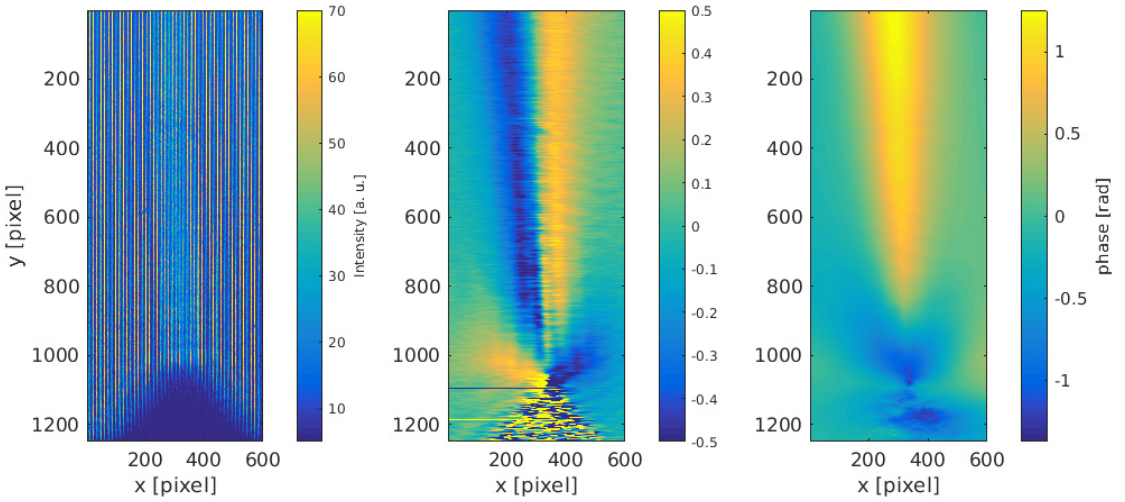

Figure 4.13: Process of the phase retrieval for a jet from the 0.2 mm nozzle imaged with the 61.5 µm amplitude grating. The image on the left is the raw object frame. In the center, the reconstructed differential phase-contrast is displayed with the color code. The right image is the absolute phase-shift obtained by integration of the differential phase-contrast image.

regions of the jet, so that the jet appears to have a different width. Rests of liquids or condensed water could also have an effect on the retrieved image. Furthermore, the gas bottle does not specify the exact contents, so it unclear whether impurities are included like an additional propellant gas or some byproduct from the manufacturing process. And finally, the reconstruction has its uncertainties as well, like an error in positioning of the sample influencing the magnification and the calculation of the integrated phase-shift. The finite grating period cannot catch the exact peaks of the differential phase-contrast, which leads to errors in the integration as well.

The evaluation of the transmission and the dark-field images is not an aspect of this thesis. Thus the process of the reconstruction is summed up in three steps, for which corresponding data is shown in Figure 4.13. First, the raw object image and the corresponding reference are selected from the data set. From this, the differential phase-contrast is reconstructed and finally, by integrating over the image in x-direction, the phase-shift in the line-of-sight is calculated.

4.4.2 Amplitude Grating

The Talbot interferometer is set up with an amplitude grating to measure the phase-shift of butane jets that emanate from nozzles of multiple diameters and with dif-

Table 4.2: Results for the amplitude grating and 4 nozzles. The diameter of the nozzles D_N is given together with the calculated thickness of the gas jet. Once calculated with the magnitude of the phase-shift D_P and once with the width D_W of the Gaussian fit functions corrected for the magnification. The errors given are the variations of the fit parameters.

D_N [mm]	D_P [mm]	D_P/D_N	D_W [mm]	D_W/D_N
0.2	0.149 ± 0.001	0.75	0.789 ± 0.003	0.25
0.4	0.225 ± 0.001	0.56	0.717 ± 0.003	0.56
0.6	0.427 ± 0.002	0.71	0.379 ± 0.002	1.6
1.0	0.787 ± 0.003	0.79	1.145 ± 0.001	0.87

ferent distances to the detector.

Thickness of the Gas Jet

To measure the refractive index with regard to the influence of the thickness of the butane gas jet, nozzles with 4 different inner diameters are placed in the laser beam at a distance of 54.4 cm to the camera. The grating is positioned 2.35 cm from the camera, which means that the detector stands in the second Talbot distance. The distance between laser focus and camera is 2.394 m.

The inner diameters of the 3D printer nozzles range from 0.2 mm to 1.0 mm, which sets high demands on the spatial resolution. Thus, the 61 µm grating is chosen for testing, since the period is small but still large enough to be captured by the camera. As described in the prior section, for each nozzle a sequence of image is measured in which the butane jet is captured multiple times. One of the object images is chosen and evaluated, meaning that the differential phase-contrast is retrieved, unwrapped and integrated before 50 succeeding lines of the resulting image are extracted, averaged and fitted by a Gaussian function. In Table 4.2, the results of this procedure are shown for the four different nozzles. For better comparability, the values from the different parameters were brought to the same physical quantity. The phase-shift integrated over the line of sight is calculated to the thickness of the sample in line-of-sight with help of the assumed refractive index. The projected width perpendicular to the line-of-sight is determined with the $1/e^2$ criterion, that is introduced in Section 4.4.1. Both values are given relative to the diameter of the nozzle in Table 4.2 as well.

Determining the thickness of the gas jet via the $1/e^2$ width yields results from 25 % to 160 % of the nozzle size. This wide range of results causes a large error margin on the average relative projected thickness which calculates to (82±60) %. The large

error margin could mean that the initial assumption, that the jet diameter scales linearly with the nozzle diameter, is wrong. However, this would not explain, why the linear scaling applies better to the thickness calculated by the phase-shift in line-of-sight. It is possible that the variation stems from fluctuations or turbulence in the jet. But while the errors of the fit parameters are not significant, the variation of the parameters from jet to jet is. So, the bad reproducibility of the jets seems to cause larger problems, than the fit itself. As mentioned, the grating has a period of 61 µm, so the 0.2 mm nozzle is covered by only 4 grating bars. This could make an exact localization of the phase-shifting gas difficult and might explain the unreliable results. But the raw data, which is for example shown in Figure 4.13, suggests that the size of the jet might be larger than the nozzle. So, the sampling is probably better than the above estimation.

The measurement of the phase-shift taken with the phase-grating estimates the thickness of the gas jet as (70±10) % of the nozzle diameter. This gives rise to the assumption that either the refractive index of the jet is smaller than expected or that the butane jets are thinner than the nozzle diameters. Another fact to consider is, that the cylindrical symmetry is only an assumption. The measurement of the 0.6 mm nozzle by determining the thickness in the line of sight D_P lies well within the average of all tested nozzles, while the determination perpendicular to the line of sight D_W yields the highest of the four results. This might be a hint, that the transverse planes of the jets are rather elliptical than circular. This could be a topic for future experiments.

Influence of the Propagation

As mentioned in Section 4.4.1, artifacts due to propagation effects are discernible in the transmission and the dark-field image. This raises the question whether the propagation distance between the sample and the detector has an influence on the detected phase-shift as well.

The phase-shift caused by the butane jets from the 1 mm nozzle is recorded in two different set-ups. The positions of the light source, the grating and the camera remains unchanged. The source and the detector have a distance of 239,4 cm to each other. The grating is placed such, that the second Talbot order is imaged. Since Z_T =1.16 cm, the size of the small camera housing is already large enough to permit imaging in the first Talbot order. However, this is regarded in the evaluation and does not cause any problems. While propagating from the object to the camera, the transverse intensity distribution of the light beam changes. To determine the influence of that phenomenon on the image reconstruction, the object is imaged at two different distances to the camera. In the 'far' measurement, the object is placed

between light source and camera at a distance of 54.4 cm to the camera. In the 'close' set-up, the distance is only 4.0 cm.

For each geometry, an image series of the gas jet was recorded. In a first step of selection, the object images of the jet that show strong turbulence are removed from the series. Jets that bend away from a straight path or seem to fluctuate are removed as well. The remaining images are reconstructed with the above described procedure. The final step is to remove the reconstructed images that show unwrapping artifacts or strong asymmetry. After this selection process, 4 reconstructed images of about 30 raw images remain for evaluation. The 'far' sample shows up with an average phase-shift of (8.50 ± 0.22) rad, where the error margin is the standard error calculated from the standard deviation. For the 'close' sample, the phase-shift calculates to (9.27 ± 0.05) rad.

The results imply that the propagation artifacts influence the phase-contrast image as well, even though they appear less obvious there than in the two other retrieved images. The error margin is significantly larger for the 'far' object, that was imaged in a more than 10 times larger distance than the 'close' sample. The propagation effects cause problems throughout the whole reconstruction process. Finding 4 suited images for the 'far' object has been more difficult than for the 'close' one. Thus, the larger error margin is not surprising. However, that the propagation distance has an influence on the average as well was not expected a priori. The measurement of the 'close' sample is nearer to the result that is expected when assuming that the refractive index of butane and that the jet has the same diameter as the nozzle.

4.4.3 Phase Grating

The measurement of the jet thickness is repeated with the phase grating. Furthermore, the influence of frequency doubling on the results of the reconstruction is evaluated.

Thickness of the Gas Jet

The measurement with multiple nozzles is repeated to allow a comparison between the amplitude and the phase grating. To this end, in the grating set-up, the detector is placed 240 cm from the light source and the 35 µm phase grating is mounted (23.5 ± 5) mm in front of the detector, so the image is taken closely to the sixth Talbot distance. The nozzles are positioned 12 cm from the camera. All seven nozzles are tested in this measurement. The results are translated to estimates of the thickness of the butane gas jet and displayed in Table 4.3. The thickness

Table 4.3: Results for the phase grating and 7 nozzles. The diameter of the nozzles D_N is given together with the jet thickness calculated with the phase-shift D_P and Gaussian width D_W. The errors given are the variations of the fit parameters.

D_N [mm]	D_P [mm]	D_P/D_N	D_W [mm]	D_W/D_N
0.2	0.144 ± 0.001	0.72	0.721 ± 0.003	0.41
0.3	0.156 ± 0.001	0.52	0.507 ± 0.002	0.59
0.4	0.197 ± 0.001	0.49	0.575 ± 0.003	0.70
0.5	0.358 ± 0.001	0.72	0.621 ± 0.001	0.81
0.6	0.247 ± 0.001	0.41	0.570 ± 0.002	1.05
0.8	0.544 ± 0.001	0.68	0.539 ± 0.002	1.48
1.0	0.752 ± 0.003	0.75	0.649 ± 0.003	1.54

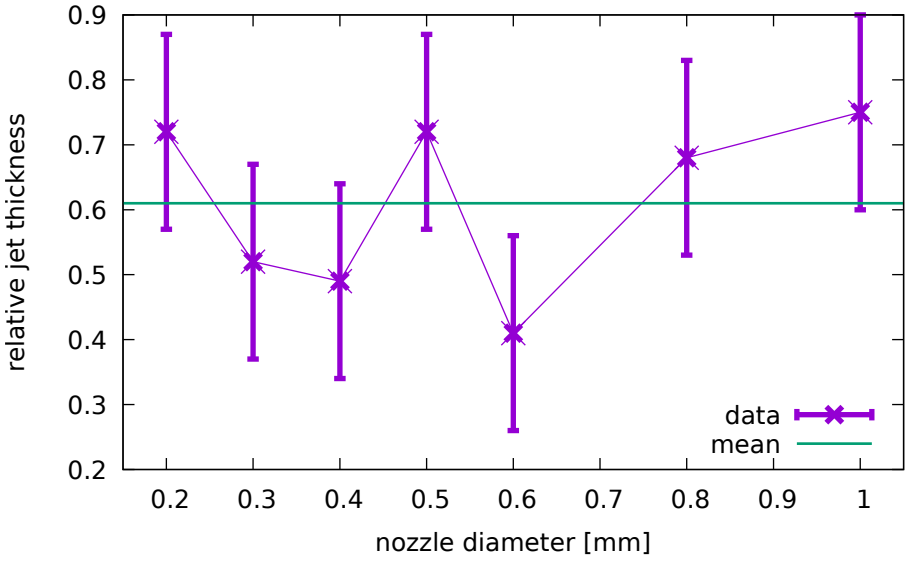

Figure 4.14: Thickness of the jets determined via phase-shift divided by the nozzle diameter plotted over the nozzle diameter. Error bars are added that represent the standard deviation and the mean value of the data is represented by the line.

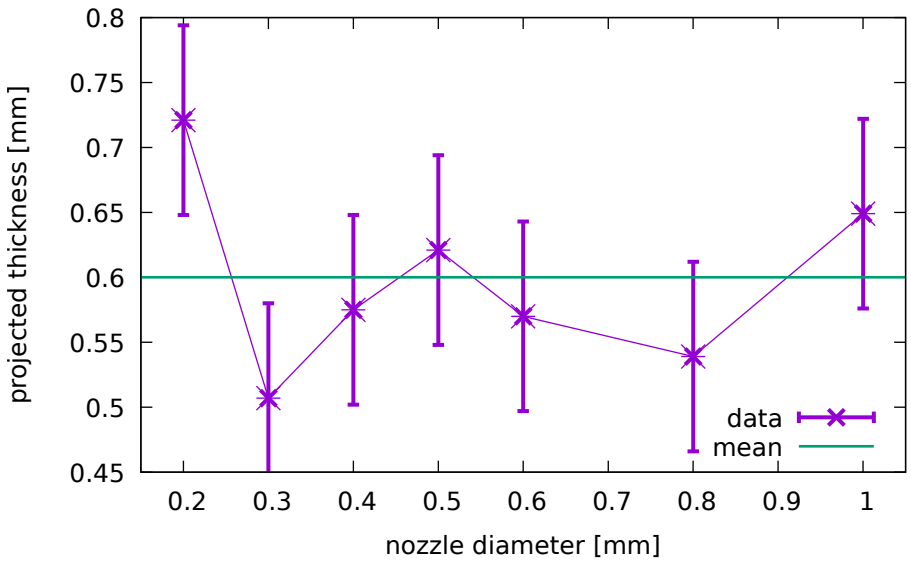

Figure 4.15: Projected thickness of the jets determined via width of the fit function plotted over the nozzle diameter. In contrast to the data in Figure 4.14, the absolute thickness is plotted instead of the relative thickness. This is done because the values show no dependency on the nozzle diameter. The error bars represent the standard deviation, a horizontal line represents the mean value.

of the butane jet in line-of-sight, which is calculated from the magnitude of the phase-shift, increases with the nozzle size as expected. The only exception from this trend is the measurement of the 0.6 mm nozzle. The relation between the calculated thickness and the nozzle size varies between 0.4 and 0.75, the mean value being 0.61. For the amplitude grating, the mean value of 0.70 is larger and fluctuates between 0.56 and 0.79 which is comparable to the fluctuation occurring with the phase grating. The thickness values calculated from the width of the distribution, in contrast, show no systematic dependency on the nozzle diameter. The average thickness value is (0.60 ± 0.08) mm. This behavior has not been observed with the amplitude grating measurement. However, it is important to keep in mind that first, the amplitude grating has an almost twice as large grating period thus limiting the spatial resolution and second, that only 4 data points were taken which makes general statements about the measurement difficult.

To better visualize the systematics of the results, the relative thickness obtained via phase-shift is plotted in Figure 4.14. It shows that the relative thickness fluctuates about the mean value without a remarkable systematic increase or decrease. In addition to that, the absolute thickness obtained via the width of the fit function is shown in Figure 4.15. It is noteworthy that this plot shows the same systematic as the prior one, even though the values were not divided by the nozzle diameter. However, the fluctuations in the plots have a certain resemblance with each other. In both plots, the values increase towards the minimum and maximum nozzle diameters while there is a local maximum at the diameter 0.5 mm. This resemblance gives the impression, that the fluctuation largely stems from the gas jet itself. It might be caused by turbulence in the jet or by variations in the gas pressure that arrives at the nozzle. Another aspect is the fact, that the phase-shift seems to increase with the nozzle diameter while the width in the lateral direction remains in a certain region. Assuming a constant refractive index, this could be interpreted such, that the spatial extent of the jet actually remains constant while the gas density rises with the nozzle size. But it is also possible, that the nozzle diameter has a large influence on the gas pressure that changes the gas temperature and thereby the refractive index. However, more detailed data would be required to look further into these hypotheses.

Frequency Doubling

Frequency doubling is introduced in Section 2.3.1 as a property of the π-shifting phase grating. It means, that the spatial frequency of the Talbot pattern is twice as high as the frequency of the grating bars. A $\pi/2$-shifting grating shows no frequency doubling. As discussed in Section 4.3, the phase depth of the grating is unknown,

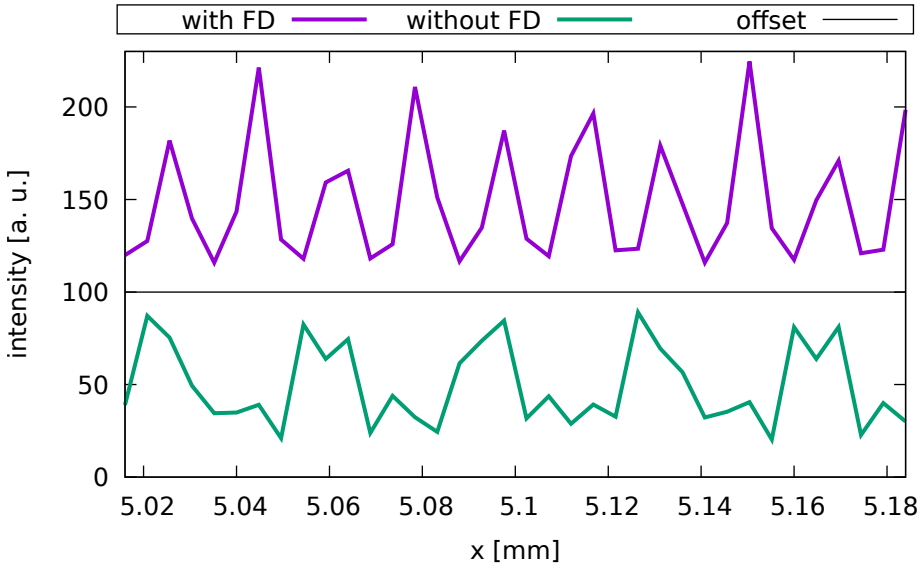

Figure 4.16: Intensity profile with (with FD) and without (without FD) frequency doubling. Plotted is a section of the reference images for the phase grating in x-direction. The upper line plot is shifted by an offset of 100 [a. u.] for better clearness. The profile contains several periods averaged over 100 lines in the central region of the detector.

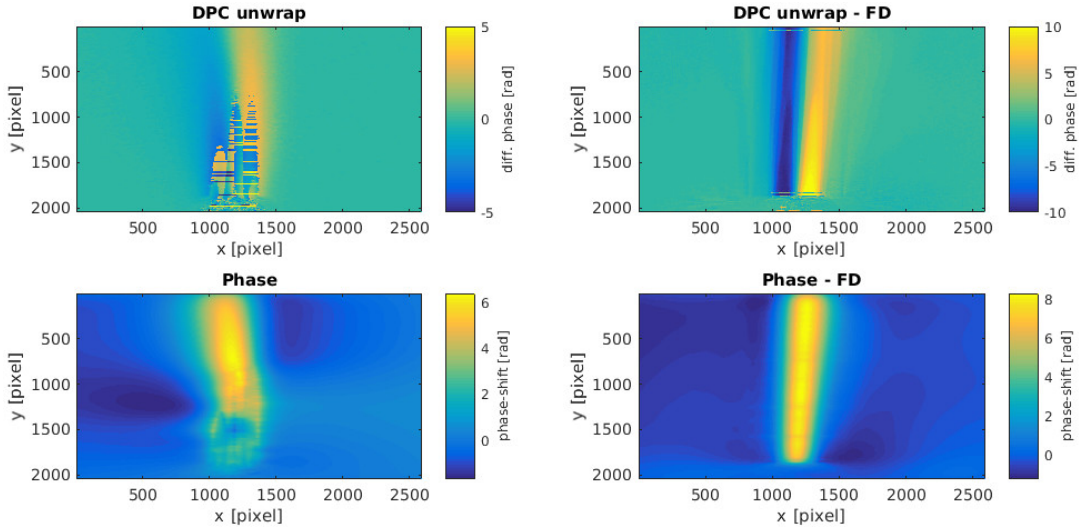

Figure 4.17: Unwrapped differential phase-contrast and phase-shift images of the gas jet from the 1.0 mm nozzle at 4.0 cm distance between the object and the detector measured with the phase grating. Data on the right is taken with frequency doubling (FD), on the left without.

but presumably neither π nor $\pi/2$ for the 650 nm laser. Thus, it is not clear whether it exhibits frequency doubling.

Figure 4.16 shows intensity profiles of reference images that were taken with the phase grating at two different z-distances between the grating and the detector. In general, the intensity profiles, that are plotted in x-direction, show an additional peak within every grating period. However, the additional peak varies in intensity. One of the profiles in Figure 4.16 is taken with the detector at a z-position, at which only one prominent peak per grating period is visible. The other profile is taken at the optimum position for frequency doubling. From that, the visibility is calculated to (65±8) % with, and to (42±1) % without frequency doubling. The error margin is calculated by an error propagation from the standard error of the peak and valley intensity values in the line profiles. The frequency doubled profile has a significantly higher visibility, but it is less uniform than the visibility of the profile without frequency doubling which shows in the larger error margin. This seems plausible because of the systematic difference in the intensity values of the frequency doubled peaks.

The consequences of the distinctive intensity profiles for the quality of the reconstructions is tested in the following experiment. The detector is set up at two different distances from the phase grating. To achieve frequency doubling, it is placed 2.37 cm behind the grating and for a measurement without frequency doubling it is positioned at 2.25 cm. On a side note, that these values cannot be compared to the z-distances given for the Talbot carpet in Figure 4.9, because there, the distance is given relative to an arbitrary position. The test object is a butane gas jet from a nozzle with an inner diameter of 1.0 mm. At both detector positions, 5 successful measurements were extracted from an image sequence. The reconstructed phase-shifts are fitted by Gaussian functions. The amplitudes of the fit functions average to a phase-shift of (8.86±0.13) rad with frequency doubling and (7.56±0.63) rad without. However, it is difficult to judge whether these differences are significant, since the shape of the single jets varies. The deviation could only be a coincidence, since it is obtained by comparing just 10 gas jets. Nevertheless, it is noteworthy that not only the phase-shift measured with frequency doubling is closer to the phase-shift of 9.54 rad that is expected for 1 mm of butane gas, but also that the error margin is smaller than the value measured without frequency doubling. A similar situation can be seen in Figure 4.17. There, the differential and the integrated phase-contrast are shown for two representative measurements, one conducted with and one without frequency doubling. Unwrapping artifacts are obvious for the measurement without frequency doubling. This leads to a significantly reduced signal in the integrated phase-shift image. On the other side, the differential phase-contrast measured with frequency doubling shows only few such artifacts and much larger values overall. While this fits to the discrepancy in the result for the averaged values presented

above, it hints at a severe problem. Since the grating period and the frequency doubling are both accounted for in the reconstruction algorithm, this discrepancy is most likely not a problem in the evaluation but rather in the procedure of the measurement or a problem with the sample itself.

4.4.4 Summary

In conclusion, a quantitative evaluation of phase-contrast in butane gas jets was conducted with a Talbot interferometer. The jet is clearly visible in the three image modalities transmission, dark-field and phase-contrast. Data reconstruction is possible with both, the amplitude and the phase grating. The gas jets are suitable as test object in the sense that the gradients of the refractive indices are on a scale that is measurable with the Talbot grating. Problems arise from the lack of reproducibility, since the jets each have a different shape. Furthermore, their actual thickness can only be estimated.

The measurements were conducted with the three grating periods, 61.5 µm for the amplitude grating, 35 µm for the phase grating and effectively 17.5 µm for the phase grating with frequency doubling. Although the sampling rate for the smallest period, with only 3.6 pixels per period, is below the limit of 6.5 pixels stated by [Gal17], it seemed to yield the most precise results. Precise statements on the image quality are difficult due to the strong variations throughout all measurements that might stem from the poor reproducibility of the gas jets. More precise knowledge of the sample could significantly improve the results for the test measurements. In future experiments, this could be achieved by finding a well understood test sample, or by checking the results with well established quantitative optical methods, like a Mach-Zehnder interferometer for instance.

4.5 In-Line Phase-Contrast

Propagation-based phase-contrast imaging is introduced for the optical regime as shadowgraphy in Section 2.3.4. But since the evaluation of the acquired data in this section is based on the methods for X-ray phase-contrast imaging, the term in-line will be used instead of shadowgraphy. After outlining the procedure of the measurement and the reconstruction in this section, the requirements on the sample position are examined, before the conducted experiments are described and the results are compared to those obtained with the Talbot interferometer.

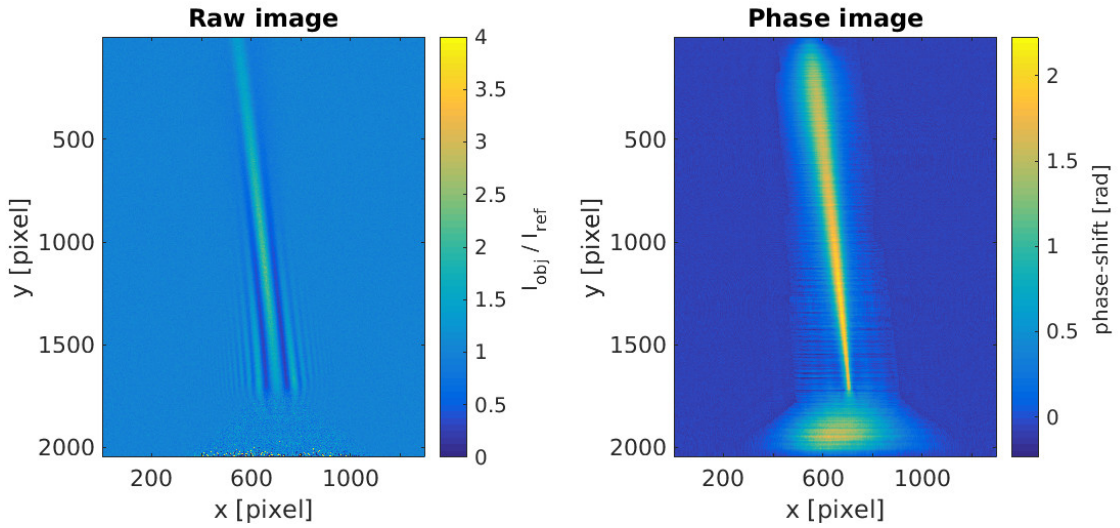

Figure 4.18: Image of the 0.2 mm nozzle as input for the in-line reconstruction algorithm on the left and the output on the right. The input is the object image divided by the reference. The color code gives the relative intensity. The output is the phase-shift integrated over the line of sight. After the reconstruction, both images have been cropped in x-direction.

4.5.1 Preliminaries

As discussed in Section 3.1, the three main components of the set-up are the light source, the test sample and the detector. An important parameter for this propagation-based technique is the propagation distance, that the laser beam covers between the sample and the detector. What needs to be considered for this is discussed in Section 4.5.2.

The input for the reconstruction is the object frame divided pixelwise by the reference. Therewith, the change that the object causes at the detector image is separated from the steady background signal. As an example, an input image of a gas jet form a 0.2 mm nozzle is shown in Figure 4.18. The jet is visible due to the intensity distribution caused by propagation effects. The intensity is increased in the central region of the jet, with vertical ripples of decreased and increased intensity enframing that region. The background around the jet is a uniform area with values ranging closely around 1. This is expected, since the object frame is normalized by the reference and both should be identical in the regions far from the object. If the jet is more turbulent, this has an influence on the appearance of the jet in the input image, as the image of a jet from the 0.6 mm nozzle shows in Figure 4.19. The image also exhibits further examples for disturbing influences. A pattern with the shape of concentric rings can be seen in center of the lower part of the input image in Figure

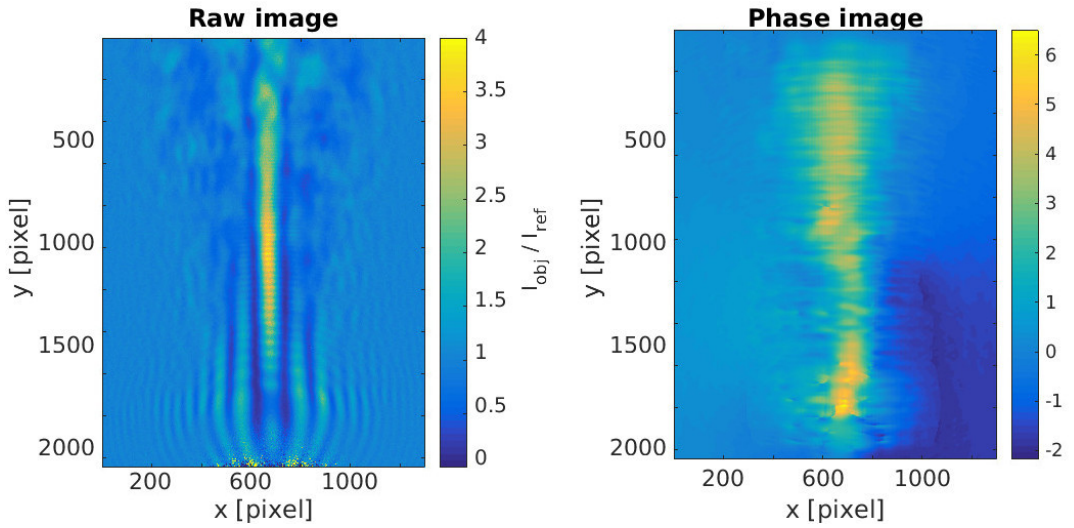

Figure 4.19: Image of the 0.6 mm nozzle as input (on the left) and output (on the right) for the in-line reconstruction. The images are cropped in x-direction. In contrast to the measurement in 4.18, a jet with more turbulence is shown. The ring shaped artifacts are visible in the cenral lower region of the input image.

4.19. The shape is similar to the thin-film interference pattern that is caused by the cover glass of the camera, which is shown in Figure 4.1. So these artifacts might be of a similar origin.

The phase-shift retrieved by the iterative algorithm is shown in the figures 4.18 and 4.19 as well. In the retrieved images, the jet stands out as an area of larger phase-shift in the center. For the jet without turbulence, the background appears homogeneous. But for the turbulent jet in Figure 4.19, the background is only uniform to the left of the jet. On the right side, especially in the lower region that is closer to the nozzle, the phase-shift value for the background drifts off to negative values. The cause for this drift can only be speculated. The drift appears to be strongest where the interference artifacts can be seen most clearly. The artifacts might be misinterpreted by the reconstruction algorithm as a phase-shifting object and thus influence the background of the image.

For both jets, horizontal stripes can be seen along the gas jet in the retrieved image. They could be due to the jet traversing the boundaries of the image frame. While the margins of the image are far from the object in the x-direction, the large extend of the jet cannot be fully captured along the symmetry axis of the jet. The influence of these artifacts might be reduced in the subsequent evaluation, by averaging the line plots, that are used for fitting, over 100 lines of the image. Such an averaged line profile can be seen in Figure 4.20 for the turbulent jet. The plot further features

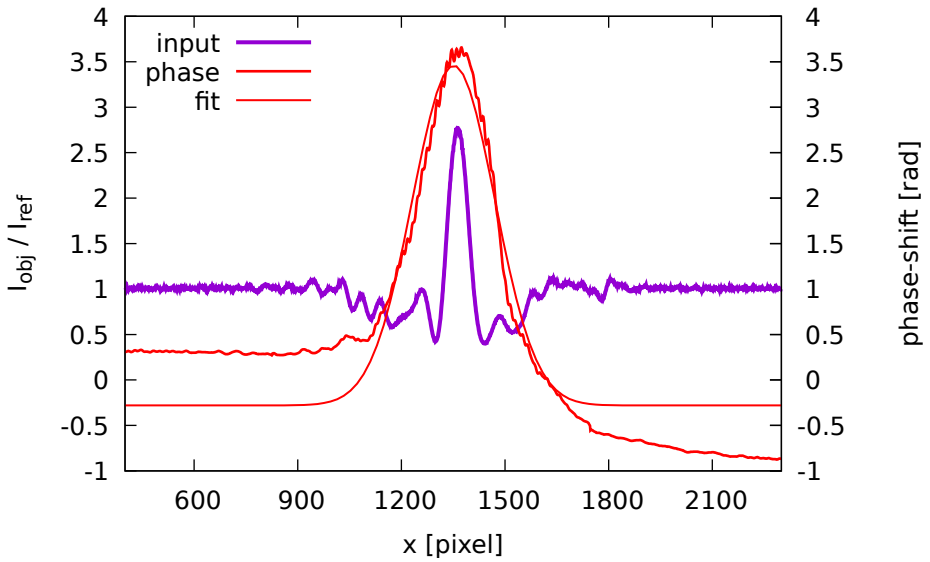

Figure 4.20: Line profiles of the input and the phase image for the 0.6 mm nozzle measured with turbulence that is shown in Figure 4.19. The profiles are averaged over the lines 600 to 700 in both, the input and the phase images. For the input, the intensity of the object image is plotted relative to the reference intensity over the number of pixels in the x-direction. For the output the reconstructed phase-shift is plotted.

an intensity profile of the input image. From the Gaussian fit to the phase-shift, an amplitude of (3.9±0.2) rad is calculated. The drift-off of the background on the right side is visible in the line plot as well. Since it is not clear, on which side the background values are more accurate, a constant offset with the average value of both sides is added to the Gaussian. For the jet in Figure 4.18, the problem with the varying background is not as severe. The jet exhibits no detectable turbulence and the thin-film interference rings cannot be seen either. The only strong artifact stems from the nozzle itself. Although it absorbs the light completely and causes no phase-shift that could actually be detected, the reconstruction algorithm calculates finite values for that region, as can be seen on the bottom of the phase image in Figure 4.20.

4.5.2 Position of the Test Sample

Since in-line phase-contrast is based on the evaluation of propagation effects that are visible in the detected image, it is important to check how much propagation distance is required so that the detected images can be evaluated. Thus, prior to data

Table 4.4: Results for the position-dependend measurement of the 1.0 mm nozzle. The phase-shift and the calculated thickness D_P in line-of-sight are shown for three different propagation distances PD.

PD [cm]	Phase-shift [rad]	D_P [mm]
4.4	5.8 ± 0.4	0.61 ± 0.04
12.0	8.8 ± 1.3	0.92 ± 0.14
54.4	8.5 ± 1.6	0.89 ± 0.17

taking, the described reconstruction procedure is applied to measure the phase-shift of the 1.0 mm nozzle at three different distances from the detector. Since the camera housing and the holder for the nozzle have a certain size, the smallest propagation distance feasible is 4.4 cm between the gas jet and the camera sensor. A medium spacing 12 cm is chosen for the intermediate position, while the largest distance is 54.4 cm. Larger distances are not regarded within the course of this experiment, since the other imaging techniques are not conducted at higher distances as well. At every of the three positions, a reference and three object images are recorded and evaluated. The average values of the resulting phase-shifts are shown in Table 4.4 together with the jet thickness in line-of-sight which is calculated from the phase-shift.

The values for the long and the medium distance approximately fit to each other and to the data taken with the Talbot interferometer, within the given margins of inaccuracy. The inaccuracy is calculated as standard error from the standard deviation of the phase-shift values obtained from each jet. Furthermore, the expected phase-shift for the 1.0 mm butane gas jet is 9.5 rad, which lies within the error margin of the measurements at 12.0 cm and at 54.4 cm. However, the expected value lies not within the error margin of the phase-shift measured at the smallest propagation distance. Since this measurement is based on a total of nine jets measured at only three distances, it is insufficient for a reliable statement. But still this measurement suggests, that 4.4 cm is not a sufficient propagation distance, while 12 cm seem to be sufficient for in-line phase-contrast measurements in this context.

4.5.3 Thickness of the Gas Jet

The experiment to measure the refractive index of the butane gas jet for the seven different inner diameters of the nozzles is repeated with in-line phase-contrast imaging. The influence of the thickness of the butane jet on the results is examined and the outcome is compared to the measurement with the Talbot interferometer.

Table 4.5: Nozzle diameter D_N with the corresponding phase-shift determined with in-line phase-contrast. D_P is the thickness in line of sight, calculated with the phase-shift.

D_N [mm]	Phase-shift [rad]	D_P [mm]	D_P/D_N
0.2	1.8 ±0.1	0.19±0.01	0.94
0.3	1.8 ±0.2	0.18±0.02	0.61
0.4	3.2 ±0.4	0.34±0.04	0.84
0.5	3.5 ±0.8	0.37±0.08	0.74
0.6	3.7 ±0.1	0.39±0.02	0.65
0.8	6.9 ±1.9	0.72±0.02	0.90
1.0	8.8 ±1.3	0.92±0.14	0.92

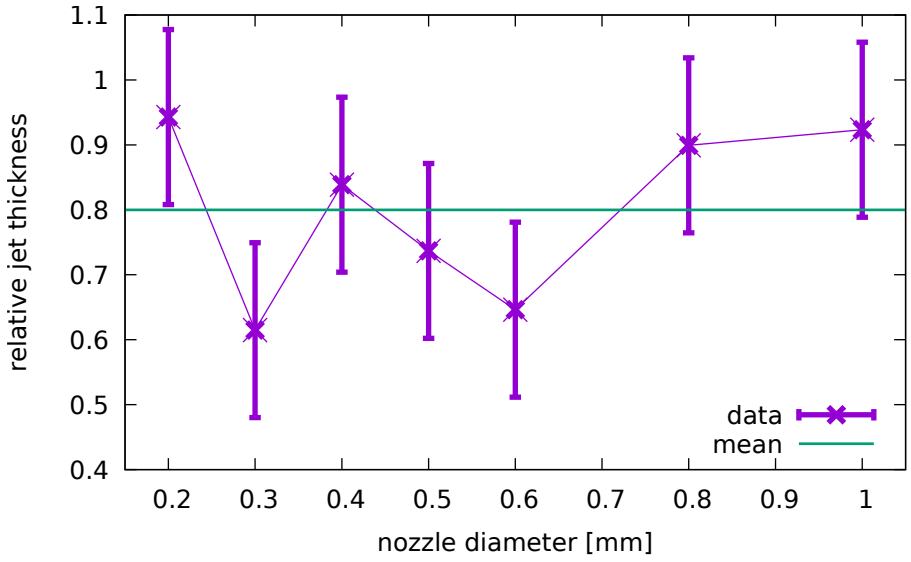

Figure 4.21: Relative jet thickness plotted over the nozzle diameter. The thickness is calculated from the phase-shift retrieved from the in-line phase-contrast measurements and divided by the nozzle diameter. The error bars represent the standard deviation. The mean value is represented by the horizontal line.

The propagation distance for this measurement is 12 cm, which is the same as the distance between the object and the detector in the thickness measurements with the Talbot interferometer described in Section 4.4.3. For every nozzle diameter, one reference and three object frames are selected from a sequence of images. The chosen frames are reconstructed and fitted as described in Section 4.5.1. From the fit parameters, the thickness of the jet is calculated by assuming a refractive index of $987{\cdot}10^{-6}$, as described in Section 3.3.3. In Table 4.5, the phase-shift and the thickness of the jet are shown with the corresponding inner diameters of the nozzle.

From the values given in Table 4.5, the jet thickness relative to the nozzle diameter calculates to an average of 0.80 ± 0.13. In comparison, the result for the corresponding measurement conducted with the phase grating with frequency doubling is (0.60 ± 0.08). A deviation of this magnitude could be due to statistical problems caused by the differences in the jet formation. The results shown in Table 4.5 are furthermore plotted in Figure 4.21. While the average value is larger than the values seen in the data presented in the figures 4.14 and 4.15, the overall appearance of the fluctuations is similar. This suggests the idea, that the different nozzles cause systematic deviations for the produced gas jets, like for example a deviation from the nominal nozzle diameter. But nonetheless, both methods have different systematic problems, as discussed in the evaluation. For example, unwrapping is a problem for the Talbot interferometer, while irregularities in the background cause problems for in-line phase-contrast. Examining and comparing the effects of the different problems more closely with a better understood test target would be a possible starting point for future experiments.

4.5.4 Summary

To sum up the experiments, propagation-based phase-contrast was observed with the optical set-up. A quantitative reconstruction was successfully applied to the recorded data to retrieve the phase-shift of the butane gas jet. By repeating the measurements conducted with the Talbot interferometer, similar results were found for the phase-shift, thus confirming the validity of both methods. However, a more precise evaluation of the in-line reconstruction requires better knowledge about properties of the test sample.

4.6 Schlieren Imaging

The third and final phase-contrast imaging technique applied in this thesis for measuring butane gas jets is Schlieren imaging. For the experiment, the laser is focused

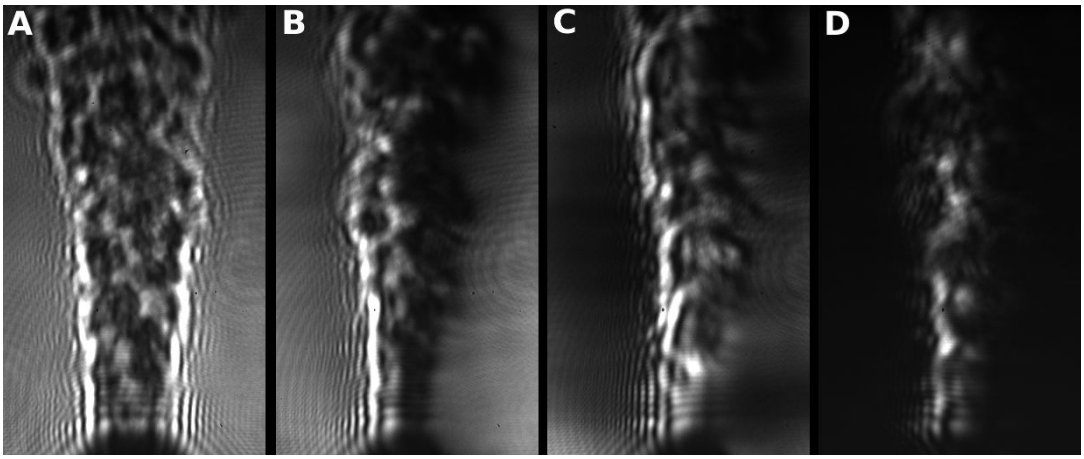

Figure 4.22: Schlieren images of the butane gas jet steming from the 1.0 mm nozzle. The images are taken without knife-edge (A), with the knife-edge covering a small part (B), a larger part and the whole (D) focal spot.

by a lens and the focal spot is cut by a knife-edge, as sketched in Figure 3.2. As introduced in Section 2.3.3, the sensitivity of the measurement depends on the focal length of the lens. Testing lenses with focal lengths ranging from 10 mm to 225 mm showed that the best results are achieved with the longest focal length. This is why all results presented here have been obtained with the 225 mm lens.

4.6.1 Position of the Knife-Edge

The distance between the source and the detector is 2.39 m, similar to the measurements for the other phase-contrast methods. The lens is placed in the laser beam at a distance of 45 cm to the detector, which is twice the focal length. The test object must be positioned in accordance with the lens Equation to produce a sharp image at the detector, as mentioned in Section 2.3.5. Thus, it is placed between the source and the lens at a distance to the lens that is approximately equal to the focal length. This is referred to as the object plane.

In contrast to the discussion in the chapters on theory and methods, the knife-edge is orientated vertically in the measurements. With this, sensitivity is achieved in the horizontal direction, which is the equivalent to the choice that was made for the direction of sensitivity for the Talbot interferometer. The knife-edge is positioned in the plane of the focal spot of the lens. There, it can be adjusted to cover the focal spot either fully, partially or not at all. The more light is blocked, the darker the image appears at the detector, which is shown in Figure 4.22 for 4 different knife-edge positions. With no knife-edge applied, the Schlieren image resembles a

shadowgraphy or a raw image for in-line phase-contrast. Close to the nozzle, the boundaries of the jet are bright fringes. As the jet streams away from the nozzle and widens in the lateral direction, this boundary becomes less distinct. Overall, the image has a vertical symmetry axis.

When applying the knife-edge to the focal spot, this symmetry is broken and the image of the gas jet changes significantly. If only a small part of the focal spot is covered, the background of the frame remains almost unchanged. The jet however, fades to black on the right side, which causes a light-and-dark contrast. As described in Section 2.3.3, the dark area in the image corresponds to areas in the object, where light is deflected by the gas jet in such a way, that it is shifted towards the knife-edge in the plane of the focal spot. The fraction of light, which is blocked that way, increases if the knife-edge is set to cover a larger part of the focal spot, as can be seen in the next image in Figure 4.22. If the spot is fully blocked, the light rays must be deflected strong enough to completely circumvent the focal spot in order to reach the detector. An image for this condition is shown in the fourth picture in Figure 4.22.

As discussed in Section 2.3.3, the light-and-dark contrast observed in the Schlieren images from the left to the right side of the gas jet corresponds to the gradient of the refractive index. Comparing for instance image B in Figure 4.22 to the data acquired with the Talbot interferometer, one sees that the the bright areas correspond to the regions of a negative differential phase-shift, while the areas of the gas jet that appear darker correspond to regions with a positive differential phase-shift. However, quantitative evaluation of the refractive index with the Schlieren system has not been conducted.

4.6.2 Additional Amplitude Grating

As suggested in Section 3.1, the Schlieren set-up can be supplemented by a Talbot grating. To this end, the amplitude grating with a period of 61.5 µm is placed in the object plane. Here, object plane refers to the area in the beam path, where objects produce sharp images at the camera sensor, as defined by the lens equation. The detector position is kept as in the prior measurements and the grating is placed closely to the object plane, so that it produces a sharp image at the detector. In this setting, the detector stands in the 45th Talbot distance.

By moving a paper card along the laser beam, the beam path can be examined qualitatively. The result of this observation is illustrated in Figure 4.23. After passing through the grating, the laser beam is focused by the lens. In the lens's focal plane, multiple light spots can be observed. For simplicity, the sketch shows

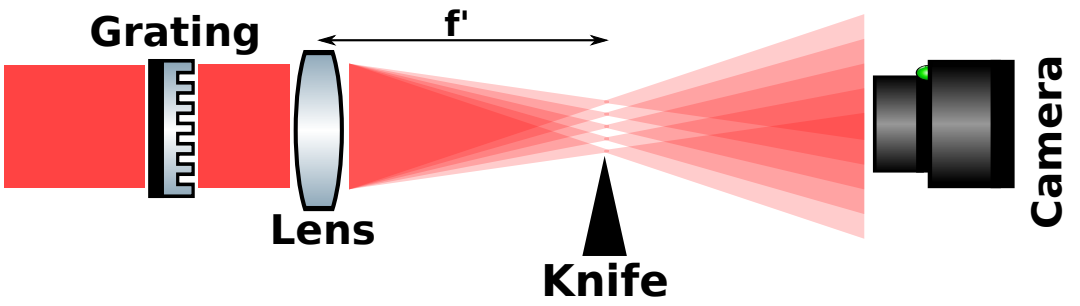

Figure 4.23: Sketch of the beam path that is observed with an amplitude grating placed in the laser beam (red) in front of the lens. The knife-edge is positioned at the effective focal length of the lens f′, where multiple focal spots can be seen. The observed beam path between lens and camera is illustrated by five semi-transparent double cones that overlay each other.

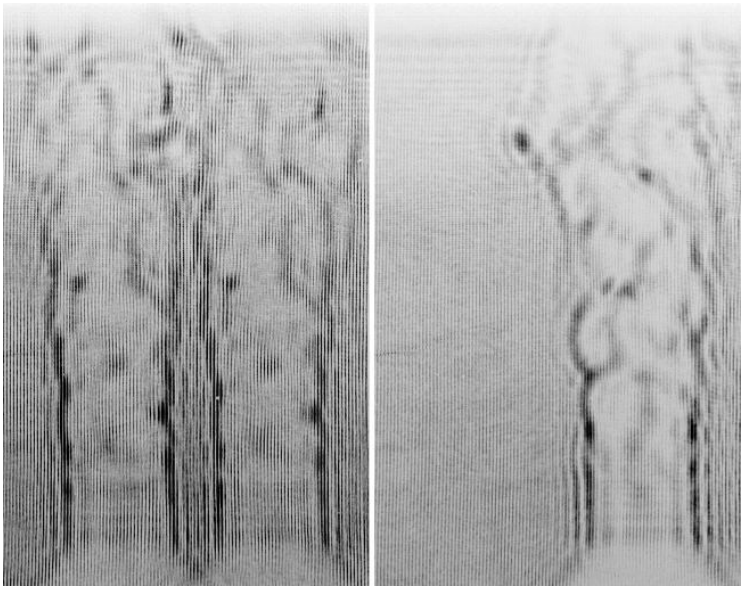

Figure 4.24: On the left, two identical instances of the object can be seen in a single image. There, the knife-edge blocks the focal spots $m_d = -\infty$ to $m_d = 0$. On the right, the knife-edge additionally blocks the spot $m_d = +1$ so that only one instance of the object remains.

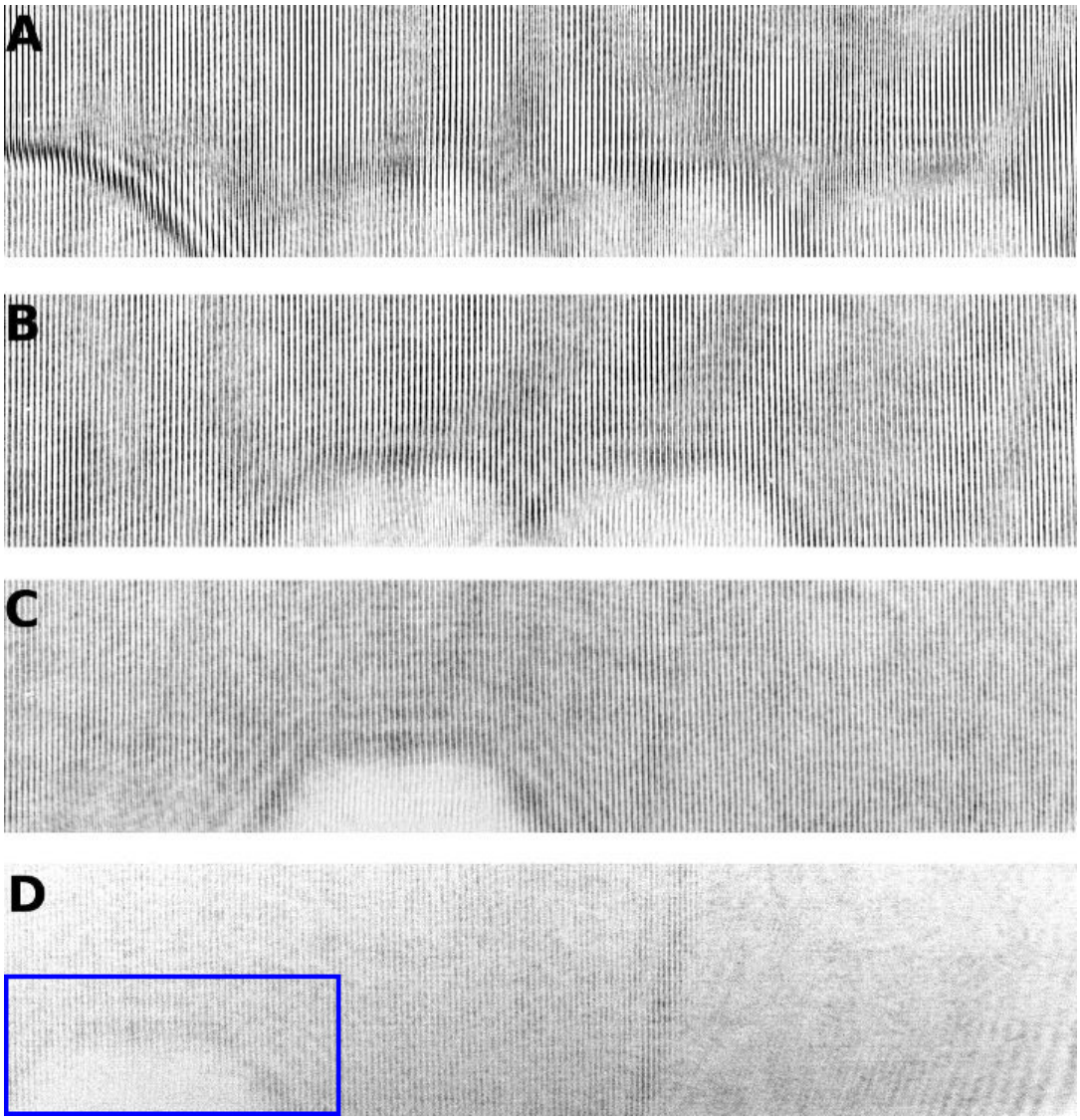

Figure 4.25: Camera images acquired by the Schlieren set-up with an additional amplitude grating. At the bottoms of the images, the 1.0 mm nozzle is seen. In A and B even multiple times. In A, the knife covers the diffraction orders $m_d = -\infty$ to $m_d = -1$. In B, $m_d = 0$ is blocked as well so that only $m_d = +1$ and higher orders are visible. In C to $m_d = +1$ is blocked as well. In D, all orders from $m_d = -\infty$ to $m_d = +2$ are blocked by the knife-edge, so that an image of the nozzle becomes visible (blue frame) that was outshined before. The brightness values in the pictures are inverted.

only five spots, even though more than that can be observed. The spots are lined up in the horizontal direction. Measuring the spacing of the spots shows, that they fulfill Equation 2.14, which describes the diffraction orders of a grating in the far field. The brightest spot is in the center and the brightness decreases for the more distant ones, as would be expected for diffraction orders of an amplitude grating. Thus, the focal spots will be named m_d, where $m_d = 0$ is the central spot and $m_d = \pm 1, 2, 3, \ldots$ for the spots to the right and left.

Since a large part of the light in the following measurements is blocked by either the grating or the knife-edge, the resulting images appear quite dark. For better clarity, the brightness values of the images are inverted. So, they are mostly bright or white and the regions where light reaches the detector appear darker or black.

An object can be placed in front of the grating, so that both are sufficiently close to the object plane. With this, a sharp image of the grating and multiple sharp images of the object can be seen by the detector. Thereby, the beam is still focused onto multiple spots between the lens and the camera. With the knife-edge, some of the spots can be blocked, while the light from the other spots can propagate on to the detector. First, the knife is set to block the spots of the orders $m_d = -\infty$ to $m_d = 0$, so that only the light from the spots $m_d = +1$ to $m_d = +\infty$ reaches the camera. A picture of the gas jet and the amplitude grating taken with this set-up can be seen in Figure 4.24. In this picture, the jet can be seen twice. Next, the spot $m_d = +1$ is blocked as well. As the second picture in Figure 4.24 shows, this has the effect that the jet can now only be seen once.

Figure 4.25 shows four pictures taken of the 1.0 mm nozzle without a gas jet. The multiple focal spots are blocked stepwise with the knife-edge, analogous to the description above. The first picture in Figure 4.25 shows the image of the nozzle threefold. There, the orders $m_d = -\infty$ to $m_d = -1$ are covered by the knife-edge. For each spot that is additionally blocked, one of the multiple images disappears, as is shown in the second and the third picture in Figure 4.25. In the fourth picture, all spots from $m_d = -\infty$ to $m_d = +2$ are blocked by the knife-edge. Thus, only the images, that are coded in the spot $m_d = +3$ and in higher spots, are still contained in the picture. Marked by a blue frame, there is an image of the nozzle that faintly shows at a position where it could only be seen faintly before. This suggests that the higher orders are present in all images, but that the lower orders outshine them so that they are not visible.

Summary

In conclusion, the Schlieren set-up presented in this section is capable of recording phase-contrast images of the butane gas jets under the same conditions that allowed

optical Talbot interferometry and in-line phase-contrast imaging. The Schlieren set-up was successfully employed to produce light-and-dark contrast that corresponds to the gradient of the refractive index in the jet. By adding an amplitude grating to the set-up, multiple copies of the imaged object were created and individually removed by properly positioning the knife-edge. In a future step, the reconstruction algorithms for Fourier imaging could be applied to attempt a quantitative evaluation of the data.

5 Summary and Outlook

This thesis is aimed at phase-contrast imaging in the visible wavelength regime. Three set-ups were characterized and tested by imaging butane gas jets, which are chosen to point towards the encountered challenges of imaging plasma targets in experiments with relevance for laboratory astrophysics.

In conclusion, an optical Talbot interferometer has been realized and characterized with both, amplitude and phase gratings. The acquired data was reconstructed and quantitatively evaluated with computational methods that were initially designed for the X-ray regime. The same was done for the method of in-line phase-contrast. The two quantitative phase-contrast methods were compared to each other and then qualitatively compared to Schlieren imaging, which is an established method for phase-contrast imaging in the optical regime. The butane jet poses challenges to the experiment in terms of reproducibility. But nevertheless, for Talbot imaging and in-line phase-contrast the obtained results for the phase-shift of the gas jet are in good agreement. With Schlieren imaging, the qualitative behavior of the gradient of the refractive index was successfully confirmed.

It is thus shown, that the presented X-ray imaging techniques can be applied to the regime of visible wavelengths as well. This poses a tool for the quantitative analysis of the refractive index of transparent media. Furthermore in future work, the optical set-up can be used to develop or to study new implementations of X-ray phase-contrast imaging methods or to validate simulations. For example, the optical set-up can help to prepare or to analyze experiments at synchrotron beamlines. Additionally, the educational aspects should be considered. The optical set-up allows to demonstrate a model experiment for an X-ray imaging technique that would otherwise not be accessible for direct observation by eye.

Bibliography

[Acc13] Accuratus Corporation: *Fused Silica, SiO2 Glass Properties*. www.accuratus.com/fused.html, 2013.

[ASA+06] Akahane, N., S. Sugawa, S. Adachi, K. Mori, T. Ishiuchi K. Mizobuchi: *A sensitivity and linearity improvement of a 100-dB dynamic range CMOS image sensor using a lateral overflow integration capacitor*. IEEE Journal of Solid-State Circuits, 41(4):851–858, April 2006.

[Bar10] Bartl, Peter: *Phasenkontrast-Bildgebung mit photonenzählenden Detektoren*. doctoral thesis, Friedrich-Alexander-Universität Erlangen-Nürnberg (FAU), 2010.

[Bas19] Basler AG: *Newton's Rings*. www.baslerweb.com/en/sales-support/knowledge-base/, 2019.

[Bec09] Bech, Martin: *X-ray imaging with a grating interferometer*. Faculty of Science, University of Copenhagen, 2009.

[BKSW10] Bennett, Eric E., Rael Kopace, Ashley F. Stein Han Wen: *A grating-based single-shot x-ray phase contrast and diffraction method for in vivo imaging*. Medical Physics, 37(11):6047–6054, 2010.

[BLT+11] Burvall, Anna, Ulf Lundström, Per A. C. Takman, Daniel H. Larsson Hans M. Hertz: *Phase retrieval in X-ray phase-contrast imaging suitable for tomography*. Opt. Express, 19(11):10359–10376, May 2011.

[Buc07] Buchwald, Kristian: *White Paper – Fused Silica Transmission Gratings*. Ibsen photonics, 2007.

[BZL+12] Bevins, Nicholas, Joseph Zambelli, Ke Li, Zhihua Qi Guang-Hong Chen: *Multicontrast x-ray computed tomography imaging using Talbot-Lau interferometry without phase stepping*. Medical Physics, 39(1):424–428, 2012.

[CER19] CERN: *Restarting the LHC: Why 13 Tev?* https://home.cern/science/engineering/restarting-lhc-why-13-tev, 2019.

[CGM+97] Cloetens, P., J. P. Guigay, C. De Martino, J. Baruchel M. Schlenker: *Fractional Talbot imaging of phase gratings with hard x rays.* Opt. Lett., 22(14):1059–1061, Jul 1997.

[Cor68] Cords, Paul H.: *A High Resolution, High Sensitivity Color Schlieren Method.* Optical Engineering, 6:6 – 6 – 4, 1968.

[CPP+10] Clark, J. N., C. T. Putkunz, M. A. Pfeifer, A. G. Peele, G. J. Williams, B. Chen, K. A. Nugent, C. Hall, W. Fullagar, S. Kim I. McNulty: *Use of a complex constraint in coherent diffractive imaging.* Opt. Express, 18(3):1981–1993, Feb 2010.

[CSJ+18] Cao, S. Q., M. G. Su, Z. H. Jiao, Q. Min, D. X. Sun, P. P. Ma, K. P. Wang C. Z. Dong: *Dynamics and density distribution of laser-produced plasma using optical interferometry.* Physics of Plasmas, 25(6):063302, 2018.

[Dem11] Demtröder, Wolfgang: *Laserspektroskopie 1.* Springer, Germany, 2011.

[Dem17] Demtröder, Wolfgang: *Experimentalphysik 2.* Springer, Germany, 2017.

[Deu99] Deutsches Museum: *Auszug aus: Meisterwerke aus dem Deutschen Museum Band II.* `www.deutsches-museum.de/sammlungen/meisterwerke/meisterwerke-ii/Roentgen/`, 1999.

[Dia18] Diabelichtung. `www.diabelichtung.info`, 2018.

[DWYT15] Da-Wei, Yuan Li Yu-Tong: *Studies of collisionless shockwaves using high-power laser pulses in laboratories.* Chinese Physics B, 24(1):015204, 2015.

[DZ18] Downer, M. C. R. Zgadzaj: *Diagnostics for plasma-based electron accelerators.* REVIEWS OF MODERN PHYSICS, 90, 2018.

[Edg69] Edgar, R.F.: *The Fresnel Diffraction Images of Periodic Structures.* Optica Acta: International Journal of Optics, 16(3):281–287, 1969.

[EGP07] E. Gamet, A. V. Tishchenko O. Parriaux: *Cancellation of the zeroth order in a phase mask by mode interplay in a high index contrast binary grating.* Appl. Opt., 46(27):6719–6726, Sep 2007.

[EKB+08] Engelhardt, M., C. Kottler, O. Bunk, C. David, C. schroer, J. Baumann, M. Schuster F. Pfeiffer: *The fractional Talbot effect in differential x-ray phase-contrast imaging for extended and polychromatic x-ray sources.* Journal of Microscopy, 232(1):145–157, 2008.

[Fiu15] Fiuza, Frederico: *Particle acceleration in shocks: from astrophysics to the laboratory in silico.* White Paper for Frontiers of Plasma Science Panel, 2015.

[Fox12] Fox, Mark: *Optische Eigenschaften von Festkoerpern.* Oldenbourg Wissenschaftsverlag GmbH, Munich, Germany, 2012.

[Gal17] Gallersdörfer, Michael: *Untersuchungen zur Nutzung des Moiré-Effektes für die gitterbasierte Phasenkontrast-Röntgenbildgebung.* Masterarbeit aus der Physik, Erlangen Centre for Astroparticle Physics, FAU, 2017.

[GKK+11] Giewekemeyer, K., S. P. Krüger, S. Kalbfleisch, M. Bartels, C. Beta T. Salditt: *X-ray propagation microscopy of biological cells using waveguides as a quasipoint source.* Phys. Rev. A, 83:023804, Feb 2011.

[Gre07] Gregory, Christopher David: *Astrophysical jet experiments with laser-produced plasmas.* 2007.

[HB02] Hsu, S. C. P. M. Bellan: *A laboratory plasma experiment for studying magnetic dynamics of accretion discs and jets.* Monthly Notices of the Royal Astronomical Society, 334(2):257–261, 2002.

[Hec14] Hecht, Eugene: *Optik.* Oldenbourg Wissenschaftsverlag GmbH, Munich, Germany, 2014.

[Hes16] Hess Collaboration: *Acceleration of petaelectronvolt protons in the Galactic Centre.* Nature, 2016.

[HS17] Hagemann, Johannes Tim Salditt: *Divide and update: towards single-shot object and probe retrieval for near-field holography.* Opt. Express, 25(18):20953–20968, Sep 2017.

[HW00] Hulbert, S.L. G.P. Williams: *Vacuum Ultraviolet Spectroscopy - Synchrotron Radiation Sources.* Academic Press, Burlington, 2000.

[Ind18a] Indian Institute of Technology Guwahati: *MEASUREMENTS IN FLUID MECHANICS Compressible Flow – Part-III.* `nptel.ac.in/courses/101103004/module7/lec7/4.html`, 2018.

[Ind18b] Indian Institute of Technology Guwahati: *MEASUREMENTS IN FLUID MECHANICS Compressible Flow – Part-III.* `nptel.ac.in/courses/101103004/module7/lec7/4.html`, 2018.

[Job95] Jobes, F. C.: *Rational Choices for the Wavelengths of a Two Color Interferometer.* 1995.

[LCB+02] Lebedev, S. V., J. P. Chittenden, F. N. Beg, S. N. Bland, A. Ciardi, D. Ampleford, S. Hughes, M. G. Haines, A. Frank, E. G. Blackman T. Gardiner: *Laboratory Astrophysics and Collimated Stellar Outflows: The Production of Radiatively Cooled Hypersonic Plasma Jets*. The Astrophysical Journal, 564(1):113, 2002.

[Lor81] Lord Rayleigh: *On copying diffraction-gratings, and on some phenomena connected therewith*. The London, Edinburgh, and Dublin Philosophical Magazine and Journal of Science, 11(67):196–205, 1881.

[Mes17] Meschede, Dieter: *Optics, Light, and Lasers*. Wiley-VCH, Weinheim, Germany, 2017.

[MGA+96] Marquès, J. R., J. P. Geindre, F. Amiranoff, P. Audebert, J. C. Gauthier, A. Antonetti G. Grillon: *Temporal and Spatial Measurements of the Electron Density Perturbation Produced in the Wake of an Ultrashort Laser Pulse*. Phys. Rev. Lett., 76:3566–3569, May 1996.

[Mic19] Micro Swiss: *MK8 Plated Wear Resistant Nozzle*. `https://store.micro-swiss.com/collections/nozzles/products/mk8`, 2019.

[Mik18] Mikhail Polyanskiy: *Refractive index database*. `www.refractiveindex.info`, 2018.

[Nav19] Nave, R.: *Thin-Lens Equation:Cartesian Convention*. hyperphysics.phy-astr.gsu.edu/hbase/geoopt/lenseq.html, 2019.

[New19a] Newport Corporation: *Mid-Range TravelSteel Linear Stages – User's Manual*. `ftp://download.newport.com/MotionControl/Archive/Positioner%20Manuals/UTM_E.pdf`, 2019.

[New19b] Newport Corporation: *Optics Formulas*. `www.newport.com/n/optics-formulas`, 2019.

[Omn18] Omnexus Special Chem: *Low and Ultra-low Refractive Index Polymers*. `https://omnexus.specialchem.com/tech-library/article/low-ultra-low-refractive-index-polymers`, 2018.

[Pag06] Paganin, David M.: *Coherent X-ray imaging*. Oxford University Press, Oxford, England, 2006.

[PPBS96] Pedrotti, F., L. Pedrotti, W. Bausch H. Schmidt: *Optik für Ingenieure*. Springer, Berlin, Germany, 1996.

[PRH+16] Park, Hye-Sook, J. S. Ross, C. M. Huntington, F. Fiuza, D. Ryutov, D. Casey, R. P. Drake, G. Fiksel, D. Froula, G. Gregori, N. L. Kugland, C. Kuranz, M. C. Levy, C. K. Li, J. Meinecke, T. Morita, R. Petrasso, C. Plechaty, B. Remington, Y. Sakawa, A Spitkovsky, H. Takabe A. B. Zylstra: *Laboratory astrophysical collisionless shock experiments on Omega and NIF*. Journal of Physics: Conference Series, 688(1):012084, 2016.

[Qua18] Quarton Inc.: *Quarton Laser Module - Adjustable focus Laser - VLM-635/650-02 Series*. `www.quarton.com/content/Laser_Module_1/Red_Laser_Module_11/Adjustable%20focus%20Laser_32/51`, 2018.

[RAP+99] Remington, Bruce A., David Arnett, R. Paul, Drake Hideaki Takabe: *Modeling Astrophysical Phenomena in the Laboratory with Intense Lasers*. Science, 284(5419):1488–1493, 1999.

[Rem05] Remington, Bruce A: *High energy density laboratory astrophysics*. Plasma Physics and Controlled Fusion, 47(5A):A191, 2005.

[Rit15] Ritter, Andre: *X-ray Talbot-Lau interferometry: Simulation and optimization*. Dissertation, Friedrich-Alexander-University Erlangen-Nürnberg, 2015.

[Rö96] Röntgen, Wilhelm Conrad: *Ueber eine neue Art von Strahlen*. Stahel, 1896.

[Sch16] Schuster, Max: *Design und Charakterisierung eines Talbot-Interferometers mit Mikrofokus-Röntgenröhre*. Masterarbeit aus der Physik, Erlangen Centre for Astroparticle Physics, FAU, 2016.

[Sci13] Scientific Polymer, Inc: *Density of Polymers by density*. `www.scientificpolymer.com/density-of-polymers-by-density`, 2013.

[Set01] Settlers, G. S.: *Schlieren and Shadowgraph Techniques*. Springer, Berlin, Germany, 2001.

[SGL+18] Seifert, Maria, Michael Gallersdörfer, Veronika Ludwig, Max Schuster, Florian Horn, Georg Pelzer, Jens Rieger, Thilo Michel Gisela Anton: *Improved Reconstruction Technique for Moiré Imaging Using an X-Ray Phase-Contrast Talbot–Lau Interferometer*. Journal of Imaging, May 2018.

[SHM+15] Schropp, Andreas, Robert Hoppe, Vivienne Meier, Jens Patommel, Frank Seiboth, Yuan Ping, Damien G. Hicks, Martha A. Beckwith, Gilbert W. Collins, Andrew Higginbotham, Justin S. Wark, Hae Ja Lee, Bob Nagler, Eric C.

Galtier, Brice Arnold, Ulf Zastrau, Jerome B. Hastings Christian G. Schroer: *Imaging Shock Waves in Diamond with Both High Temporal and Spatial Resolution at an XFEL.* Scientific Reports, 2015.

[SLG+18] Seifert, Maria, Veronika Ludwig, Michael Gallersdörfer, Christian Hauke, Katharina Hellbach, Florian Horn, Georg Pelzer, Marcus Radicke, Jens Rieger, Sven-Martin Sutter, Thilo Michel Gisela Anton: *Single-shot Talbot–Lau x-ray dark-field imaging of a porcine lung applying the moiré imaging approach.* Physics in Medicine Biology, 63(18):185010, 2018.

[Sta08] Stark Labs: *Gain, Offset, and Bit Depth.* `www.stark-labs.com/help/blog/files/GainAndOffset.php`, 2008.

[Sul97] Suleski, Thomas J.: *Generation of Lohmann images from binary-phase Talbot array illuminators.* Appl. Opt., 36(20):4686–4691, Jul 1997.

[SWX+11] Song, Xin-Bing, Hai-Bo Wang, Jun Xiong, Kaige Wang, Xiangdong Zhang, Kai-Hong Luo Ling-An Wu: *Experimental Observation of Quantum Talbot Effects.* Phys. Rev. Lett., 107:033902, Jul 2011.

[Tal36] Talbot, H.F.: *LXXVI. Facts relating to optical science. No. IV.* The London, Edinburgh, and Dublin Philosophical Magazine and Journal of Science, 9(56):401–407, 1836.

[The18] The Imaging Source: *GigE Cam DMK 33GP5000e Camera Specification Sheet.* `www.s1-dl.theimagingsource.com/api/2.5/packages/documentation/manuals-trm/trmdmk33gp5000e/c8bfd3eb-547a-503f-846f-d85add8b950d/trmdmk33gp5000e.en_US.pdf`, 2018.

[Tho18] Thorlabs GmbH: *Diffraction Gratings Tutorial.* `https://www.thorlabs.com/newgrouppage9.cfm?objectgroup_id=1122`, 2018.

[TIK82] Takeda, Mitsuo, Hideki Ina Seiji Kobayashi: *Fourier-transform method of fringe-pattern analysis for computer-based topography and interferometry.* OSA, 1982.

[VSF13] Valdivia, M. P., D. Stutman M. Finkenthal: *Talbot-Lau based Moiré deflectometry with non-coherent sources as potential High Energy Density plasma diagnostic.* Journal of Applied Physics, 114(16):163302, 2013.

[WAC+04] Woolsey, N C, A D Ash, D M Chambers, C Courtois, R O Dendy, R A D Grundy K G McClements: *Supernova remnant relevant laser-plasma experiments*. 73–80, 2004.

[WDD+05] Weitkamp, Timm, Ana Diaz, Christian David, Franz Pfeiffer, Marco Stampanoni, Peter Cloetens Eric Ziegler: *X-ray phase imaging with a grating interferometer*. Opt. Express, 13(16):6296–6304, Aug 2005.

[WF97] Weber, B. V. S. F. Fulghum: *A high sensitivity two-color interferometer for pulsed power plasmas*. Review of Scientific Instruments, 68(2):1227–1232, 1997.

[WGG+96] Wilkins, S.W., T. E. Gureyev, D. Gao, A. Pogany A.W. Stevenson: *Phase-contrast imaging using polychromatic hard X-rays*. Nature, 1996.

[WRD36] Watson, H. E., K. L. Ramaswamy F. G. Donnan: *The refractive index dispersion and polarization of gases*. 1936.

[Yor11] York, Timothy: *Fundamentals of Image Sensor Performance*. `www.cse.wustl.edu/~jain/cse567-11/ftp/imgsens/index.html`, 2011.

[YWL15] Yan, Aimin, Xizeng Wu Hong Liu: *A general theory of interference fringes in x-ray phase grating imaging*. Medical physics, 42(6):3036—3047, June 2015.

Acknowledgement

While procrastinating from finalizing the thesis in the last days of its making, I would like to dedicate this page to the ones who contributed to the completion of this oeuvre.

- Prof. Dr. Stefan Funk, for the assignment and the supervision of this thesis,
- Prof. Dr. Gisela Anton, for all the help, ideas and scientific input for the experiment,
- Max, for supervising this thesis and proofreading it especially in the stressful final week, for always being there when help is needed and last but not least for the fascinating insights to this group, the interesting projects and the splendid work atmosphere,
- Andi, for taking so much time to show me his scripts, answering every question I could think of and for the good working climate we have in our office,
- Vroni, Maria, Mareike, Dani, Julian and Tim for helping with the experiments, with the simulations and reconstructions, for various discussions and the joyful business trips,
- Florian Dötzer, Prof. Dr. Norbert Lindlein and his work group for letting us borrow the phase gratings for such a long time,
- Irina Harder, Ang Li, Alexander Tafel and Johannes Illmer for discussing ways of manufacturing or buying phase gratings and for hinting to Prof. Lindlein,
- Kay Graf and the members of the technical staff of ECAP for making the experiment possible in the first place,
- Judith, Caro and Wolfi for proofreading the most fascinating parts of my thesis, and finally
- Flo, my Family and my Friends for always being there and giving me the love and support that I need.

Erklärung

Hiermit bestätige ich, Bernhard Akstaller, dass ich diese Arbeit selbstständig und nur unter Verwendung der angegebenen Hilfsmittel und Quellen angefertigt habe.

Erlangen, den 28. 02. 2019

Bernhard Akstaller